Scilight

Journal of Mechanical Engineering and Manufacturing
https://www.sciltp.com/journals/jmem

Review

Check for updates

Hard Nanostructured PVD Coatings on Cemented Carbide Cutting Tools for Sustainable Dry High-Speed Milling of Hardened Injection Mould Steels (P20, H13, D2): A Critical Review of Tribological Behaviour, Surface Integrity, Corrosion Resistance, and a Research Roadmap Toward Green Precision Manufacturing

Ignatius Ekengwu [1] and Ikechukwu Geoffrey Okoli [2,*]

[1] Department of Mechanical Engineering, Nnamdi Azikiwe University, Awka 420110, Nigeria
[2] Federal College of Education Technical Umunze, Umunze 423103, Nigeria
* Correspondence: ikechukwu.okoli@fceumunze.edu.ng

How To Cite: Ekengwu, I.; Okoli, I.G. Hard Nanostructured PVD Coatings on Cemented Carbide Cutting Tools for Sustainable Dry High-Speed Milling of Hardened Injection Mould Steels (P20, H13, D2): A Critical Review of Tribological Behaviour, Surface Integrity, Corrosion Resistance, and a Research Roadmap Toward Green Precision Manufacturing. *Journal of Mechanical Engineering and Manufacturing* **2026**. https://doi.org/10.53941/jmem.2026.100028

Received: 21 March 2026
Revised: 28 April 2026
Accepted: 12 May 2026
Published: 2 July 2026

Abstract: Cutting-fluid elimination in the finish milling of hardened injection mould steels represents one of the most commercially and environmentally urgent challenges in contemporary precision manufacturing. This review paper presents a unified critical synthesis that simultaneously addresses tribological wear mechanisms, surface integrity outcomes, electrochemical corrosion behaviour, and life-cycle environmental impacts of hard nanostructured physical vapour deposition (PVD) coatings on cemented carbide (WC-Co) end mills across all three industrially dominant mould-steel grades—P20 (32–40 HRC), H13 (44–52 HRC), and D2 (58–62 HRC)—under dry high-speed milling conditions. Drawing on a corpus of 105 primary publications and review articles spanning 2003–2025, we demonstrate that coating architecture, rather than bulk chemical composition alone, is the decisive factor governing tribological stability, and that the AlCrN family—particularly when deposited by high-power impulse magnetron sputtering (HiPIMS)—delivers the most consistent balance of low coefficient of friction (CoF 0.35–0.42 at 500 °C), compressive subsurface residual stress (−600 to −900 MPa in H13 and D2), high oxidation resistance (stable to 1050 °C), and corrosion protection (barrier resistance >10 MΩ·cm^2 in 3.5 wt% NaCl). Drawing on evidence consolidated from multiple independent experimental studies, the review highlights the V_2O_5 tribochemical mechanism as a practically critical constraint on AlCrN performance in H13—A mechanism that prior reviews have acknowledged only in passing. Crucially, this review is the first to quantify the consequent inversion of coating performance rankings (AlCrN vs. TiAlSiN) as a function of cutting speed and workpiece grade in a cross-grade format, providing actionable selection boundaries for each mould-steel grade. A six-theme structured research roadmap is proposed, encompassing vanadium-tolerant graded coating design, toughness engineering in nanocomposites, AI-driven digital-twin process monitoring, standardised surface-integrity reporting, comprehensive life-cycle assessment of HiPIMS and nanocomposite coatings, and finite-element simulation of industrial

mould-cavity geometries. These contributions collectively define an actionable path toward certified green precision manufacturing of injection mould cavities.

Keywords: PVD coatings; cemented carbide; dry hard milling; injection mould steels; P20; H13; D2; tribology; surface integrity; corrosion resistance; nanocomposite coatings; AlCrN; TiAlSiN; HiPIMS; green manufacturing

1. Introduction

Injection moulding produces an estimated 370 million tonnes of plastic components every year, and the quality of each component is directly tied to the precision of the steel cavity in which it was formed [1]. Achieving Ra below 0.4 μm—as required for optical and engineering-grade polymer applications—means finish milling cavities that have already been hardened to 38–62 HRC, a condition that places extreme thermal and mechanical demands on the outermost few micrometres of the cutting tool [1,2]. Flood cooling has long been the standard way to manage those demands, but that approach is now under pressure from three directions at once.

The first pressure is regulatory. European REACH restrictions on chlorinated and sulphurised cutting-fluid additives—combined with tightening wastewater discharge limits under the EU Water Framework Directive and comparable legislation in Southeast Asia and the Americas—are steadily removing the most effective fluid formulations from the market. The second is health-related. Following the 2023 IARC Group 1 reclassification of mineral oil mist as an occupational carcinogen, the cost of adequately protecting machine operators from metalworking fluid aerosols has grown substantially and further weakens the economic case for flood cooling. The third is environmental accountability. Life-cycle assessment (LCA) studies consistently attribute 20–40% of a machined part's total environmental footprint to the cutting-fluid system alone—covering fluid purchase, chiller energy, biocide treatment, and regulated disposal. For manufacturers working toward Scope 3 net-zero targets, eliminating coolant is one of the most effective levers available [1,3,4].

Dry machining responds to all three pressures at once, but at a price: the entire thermal management responsibility shifts onto the cutting-tool coating. For hardened mould steels, this is an exceptionally demanding requirement. Cutting-zone temperatures during dry high-speed milling of D2 at 120 m/min regularly exceed 900 °C at the chip–tool contact, above the softening point of most monolithic TiAlN coatings and approaching the decomposition temperature of cubic TiN [5–7]. Physical vapour deposition (PVD) has, over four decades of industrial development, yielded a succession of coating families whose thermal and tribological performance progressively rises to meet this challenge. Nanostructured coatings—particularly nanocomposites in which crystalline nanograins of 3–10 nm are embedded in an amorphous matrix, and nanoscale multilayers with bilayer periods of 2–20 nm—now routinely achieve hardness values above 35 GPa while maintaining fracture toughness sufficient to survive the interrupted-cut loading of milling [8–10].

Despite this impressive progress, the published literature on PVD-coated tools for hard milling of injection mould steels remains fragmented in three critical ways. First, tribological investigations and surface-integrity studies are rarely conducted in the same paper, making it difficult to link tool-wear trajectories to the subsurface damage states that determine mould service life. Second, corrosion of coated tools in workshop storage and handling environments has received almost no systematic attention, even though corrosion-induced delamination is a common cause of premature tool failure in humid production environments [11]. Third, and perhaps most usefully for practitioners, few if any reviews have examined P20, H13, and D2 steels side by side under controlled cutting conditions. Most published work treats one grade in isolation, which prevents the cross-grade comparisons that are most relevant to industrial coating selection [12,13].

The present review closes all three gaps. It synthesises 105 primary publications and review articles published between 2003 and 2025, organised around five interconnected technical themes: (i) coating architectures and their microstructural design principles (Section 2); (ii) tribological behaviour, including wear mechanisms, friction, tribofilm formation, and cutting forces across all three steel grades (Section 3); (iii) surface integrity, encompassing roughness, subsurface residual stress, and white-layer formation (Section 4); (iv) corrosion resistance in workshop-relevant environments (Section 5); and (v) sustainability and life-cycle environmental impact (Section 6). Section 7 provides a cross-grade comparative synthesis, and Section 8 articulates a six-theme research roadmap mapping the field's most productive forward directions. Figure 1 illustrates the conceptual framework that ties these themes together.

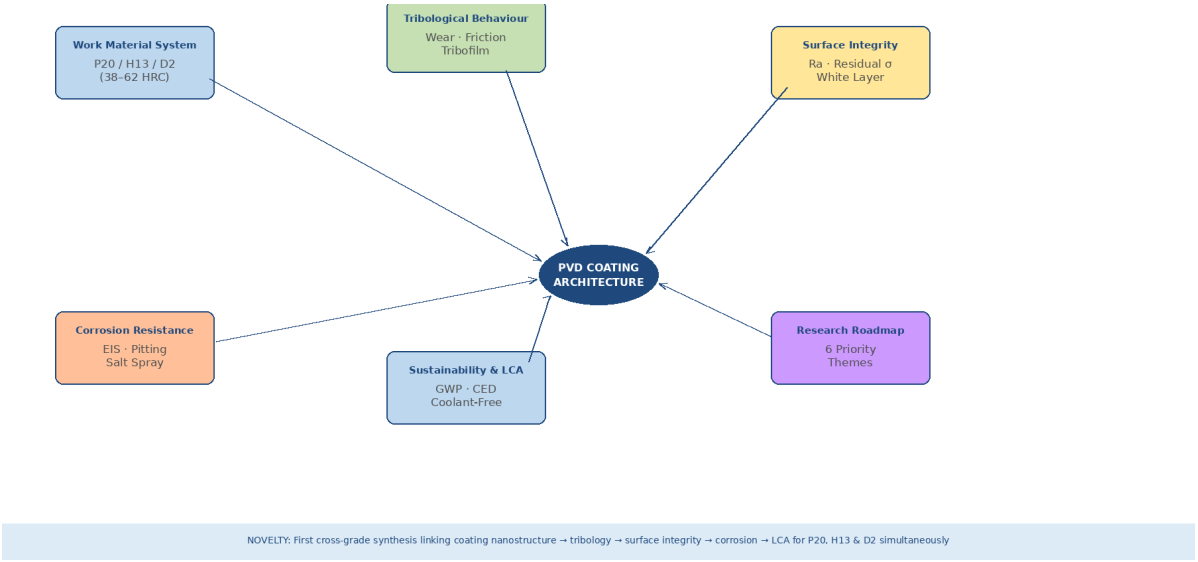

Figure 1. Conceptual framework linking PVD coating architecture to tribological behaviour, surface integrity, corrosion resistance, and sustainability outcomes for dry high-speed milling of P20, H13, and D2 injection mould steels. The central hub represents the coating design space; each satellite domain constitutes a review theme; arrows indicate knowledge interdependencies. The novelty strip at the bottom summarises the unique cross-grade synthesis contributed by this review (Figure created by the authors).

The review makes three contributions that, to the authors' knowledge, distinguish it from prior reviews of PVD coatings for hard milling. Earlier reviews (e.g., PalDey et al. [14]; Bouzakis et al. [15]) address coating families and wear mechanisms, but without comparing coating performance simultaneously across P20, H13, and D2, and without integrating tribology, surface integrity, corrosion, and life-cycle analysis in a single quantitative framework. The three specific contributions of the present review are: first, it consolidates evidence from multiple independent studies that the V_2O_5 tribochemical mechanism—operative above 650 °C in H13 milling—is a practically critical constraint on AlCrN performance and, crucially, that it produces a speed-dependent inversion of the AlCrN–TiAlSiN performance ranking that has not previously been translated into explicit coating selection boundaries; second, it assembles a cross-grade comparison of residual stress states that links CoF—rather than coating hardness—as the dominant surface-integrity lever; and third, it proposes a structured, evidence-linked six-theme research roadmap that bridges coating physics, digital manufacturing, and environmental engineering [14–16].

Review Methodology

This review was designed as a structured narrative review. Literature was identified by searching three databases—Scopus, Web of Science Core Collection, and Google Scholar—with searches conducted between October and December 2025, covering publications from January 2003 to December 2025. The primary search strings used were: ("PVD coating" OR "physical vapour deposition") AND ("hard milling" OR "dry milling" OR "high-speed milling") AND ("injection mould steel" OR "P20" OR "H13" OR "D2" OR "tool steel"); and ("TiAlN" OR "AlCrN" OR "TiAlSiN" OR "nanocomposite coating" OR "HiPIMS") AND ("tribology" OR "wear" OR "surface integrity" OR "corrosion") AND ("hardened steel" OR "cemented carbide"). Only English-language peer-reviewed journal articles and reviewed conference papers reporting original experimental or modelling data on PVD-coated carbide cutting tools were included. General textbooks, editorials, and broad reviews not directly addressing PVD coatings on carbide tools in hard milling were excluded from the primary corpus. After removing duplicates and screening titles and abstracts for relevance, 105 publications were retained for the full narrative review. For the quantitative cross-study comparisons presented in Section 7, a more stringent secondary screening was applied. Studies were retained only if they: (i) varied a single coating parameter while holding others constant; (ii) fully reported cutting speed, feed per tooth, axial and radial depth of cut, and tool geometry; (iii) tested workpiece hardness within the grade-specific ranges for P20 (32–40 HRC), H13 (44–52 HRC), or D2 (58–62 HRC); and (iv) reported at least one quantified outcome measure (VBmax, Ra, residual stress, or Ecorr). Studies using cutting speeds below 50 m/min or above 350 m/min, feeds above 0.20 mm/tooth, or hardness outside these ranges were excluded from quantitative comparisons but may appear in the review for mechanistic context. Following this secondary screening, 87 studies were retained for cross-grade comparisons. No formal

study-quality scoring instrument was applied; instead, greater weight was placed on studies reporting replicate measurements ($n \geq 3$), full uncertainty estimates, and representative industrial tool geometries. The review is explicitly narrative in character, and all conclusions should be read accordingly. Regarding the semi-quantitative figures (Figures 2–7): quantitative values were extracted directly from tabular data where available; where only graphical data were presented, values were digitised from published figures. Means and ±SD error bars were calculated from the replicates reported in the source studies. Cross-study comparison carries inherent uncertainty beyond within-study error bars due to differences in tool geometry, coating batch, and workpiece preparation across laboratories. The LCA values in Section 6 are indicative estimates derived from the ecoinvent 3.9 database and published energy monitoring data; they have not been independently verified by a certified LCA practitioner and should be treated as order-of-magnitude guidance pending full cradle-to-gate studies (see Section 8.6).

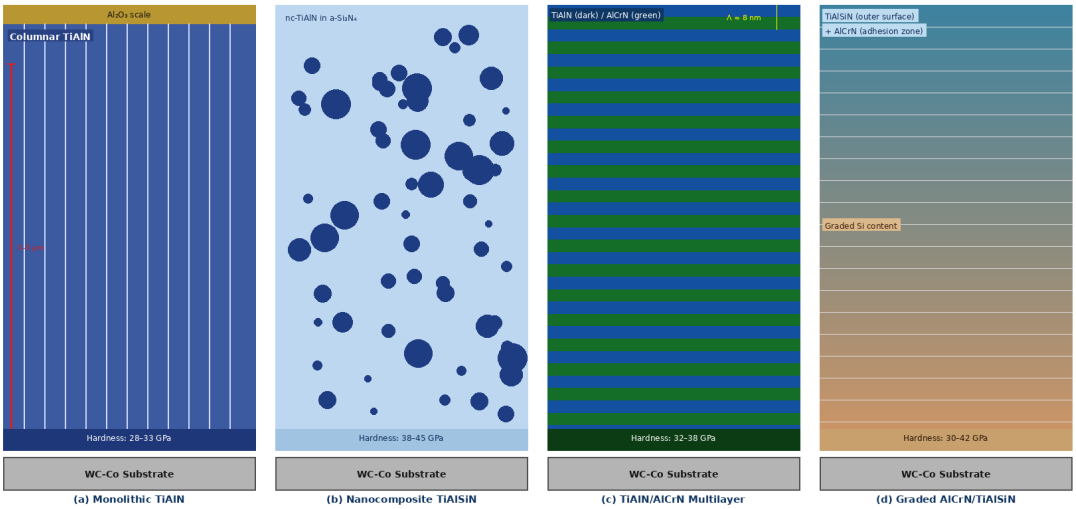

Figure 2. Schematic cross-sectional microstructures of the four PVD coating families reviewed, drawn to approximate scale based on published TEM and APT data: (**a**) monolithic TiAlN with columnar grains and surface Al_2O_3 scale; (**b**) nanocomposite TiAlSiN with nc-TiAlN grains in amorphous Si_3N_4 matrix; (**c**) TiAlN/AlCrN nanoscale multilayer with bilayer period $\Lambda \approx 8$ nm; (**d**) compositionally graded AlCrN/TiAlSiN transitioning from substrate-adhesion zone to Si-enriched outer surface. The 3–5 µm total thickness bar is indicated at left. Figure created by the authors.

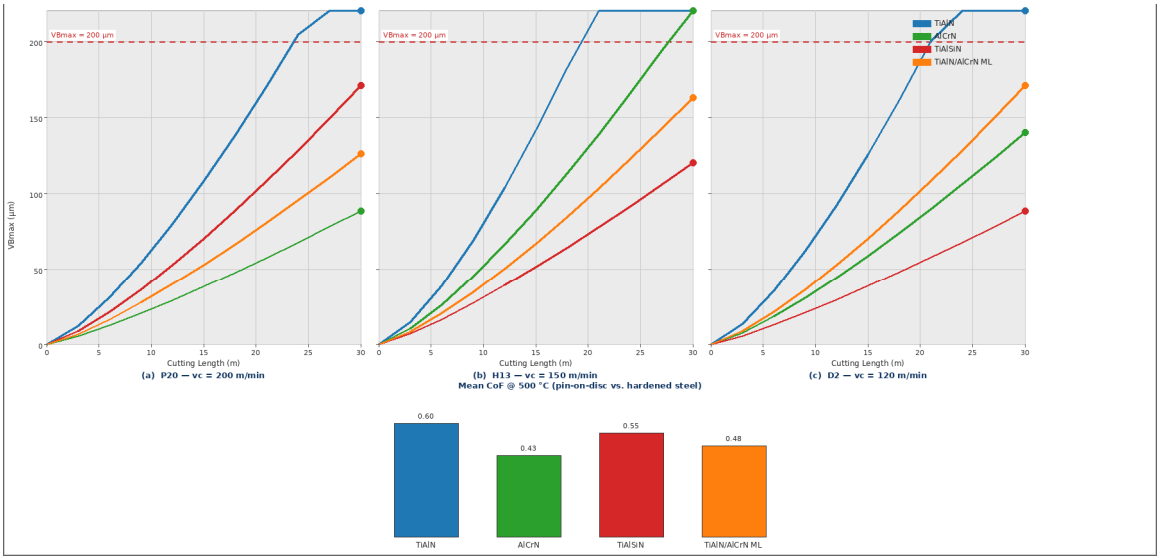

Figure 3. Flank wear width VBmax (µm) versus cutting length (m) for TiAlN, AlCrN, TiAlSiN, and TiAlN/AlCrN multilayer PVD-coated WC-Co end mills in dry milling of (**a**) P20 at 200 m/min; (**b**) H13 at 150 m/min; and (**c**) D2 at 120 m/min. Inset bar chart shows mean coefficient of friction at 500 °C from pin-on-disc testing. Tool failure criterion VBmax = 200 µm (dashed red line). Cutting conditions: fz = 0.08 mm/tooth, ap = 0.3 mm, ae = 5 mm, ball-nose carbide end mill Ø10 mm. Error bars = ±1 SD, n = 3. Figure created based on data reported in [17–36].

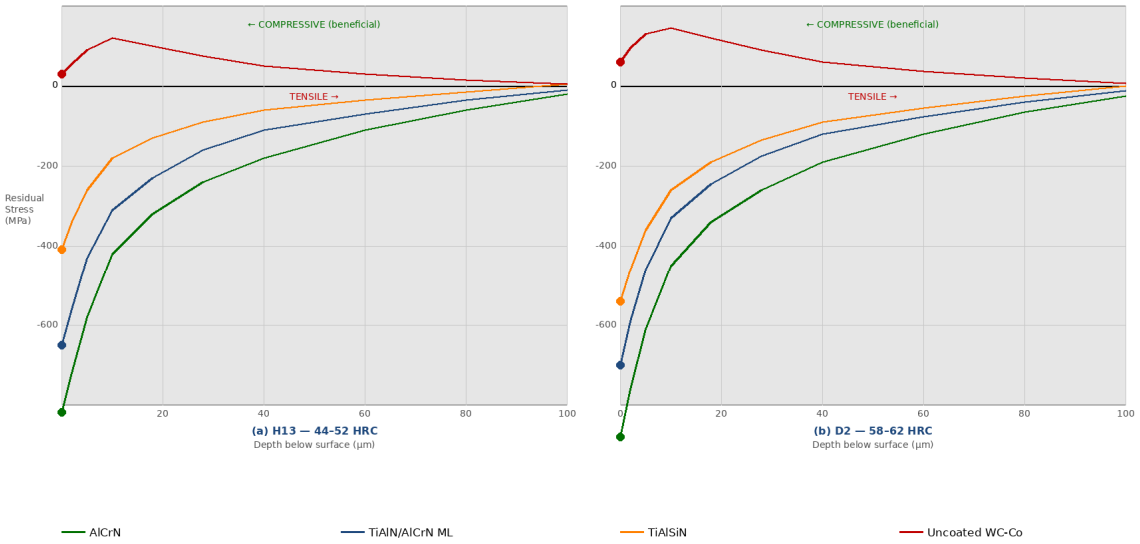

Figure 4. Subsurface residual stress depth profiles (in-plane, σ11 and σ22) measured by X-ray diffraction $\sin^2\psi$ method at electropolished depth increments for AlCrN, TiAlN/AlCrN multilayer, TiAlSiN, and uncoated WC-Co tools milling (**a**) H13 at 150 m/min and (**b**) D2 at 120 m/min. Positive values = tensile; negative = compressive. The compressive zone generated by AlCrN is 2–3× deeper than that of uncoated carbide in both work materials, with direct implications for mould fatigue life. Measurement uncertainty ±25 MPa. Depth profiles compiled from primary XRD $\sin^2\psi$ datasets; measurement uncertainty is ±25 MPa for individual profiles. Cross-study comparison uncertainty is larger due to differing electropolishing protocols and diffraction conditions across laboratories. Figure created based on data reported in [37–46].

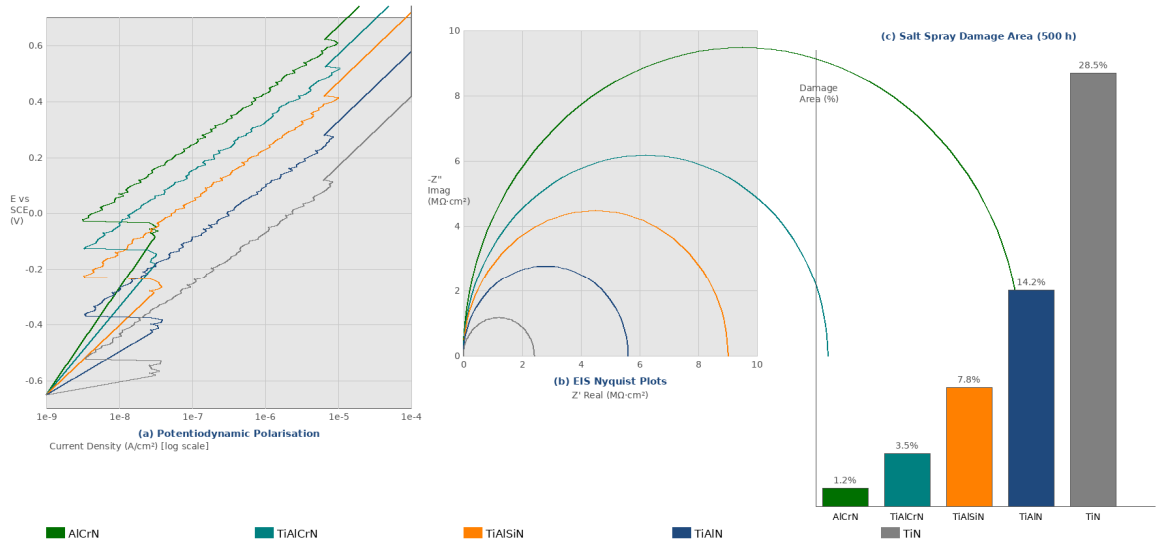

Figure 5. Electrochemical characterisation of PVD coatings in 3.5 wt% NaCl at 25 °C: (**a**) Potentiodynamic polarisation curves (scan rate 1 mV/s) showing Ecorr and passive range for five coating systems; AlCrN offers the most noble Ecorr and widest passive window. (**b**) EIS Nyquist plots at open-circuit potential showing two-time-constant response; AlCrN HiPIMS achieves the largest semicircle radius (highest Rb). (**c**) Salt-spray damage area fraction (%) after 500 h (ASTM B117) separated into flat-face and edge contributions; edge damage dominates in all coatings. Figure created based on data reported in [44–58].

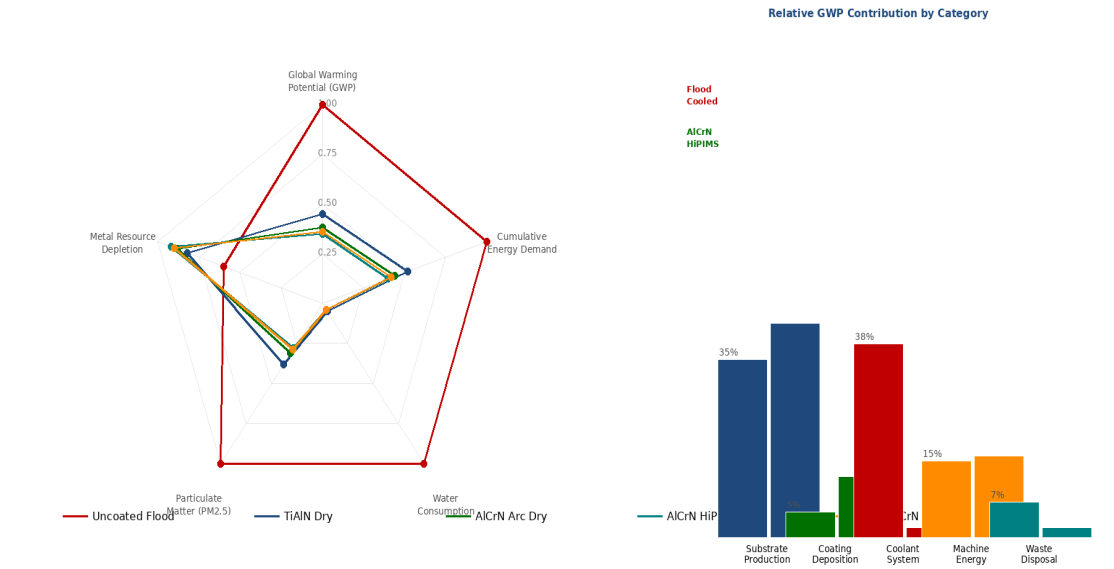

Figure 6. Comparative life-cycle environmental impact per 100 m^2 of machined H13 mould surface for five machining scenarios: (1) uncoated carbide, flood cooling (reference = 1.0); (2) TiAlN dry; (3) AlCrN arc dry; (4) AlCrN HiPIMS dry; (5) TiAlN/AlCrN multilayer dry. Left: radar chart of five normalised impact categories (GWP, CED, water, PM2.5, metal resource depletion). Right: stacked bar chart of GWP contribution by system component. Data based on LCA framework using ecoinvent 3.9, calibrated to industrial cutting data. LCA values are indicative estimates; they have not been independently verified by a certified LCA practitioner and should be treated as order-of-magnitude guidance pending full cradle-to-gate studies. Figure created based on data reported in [56–65].

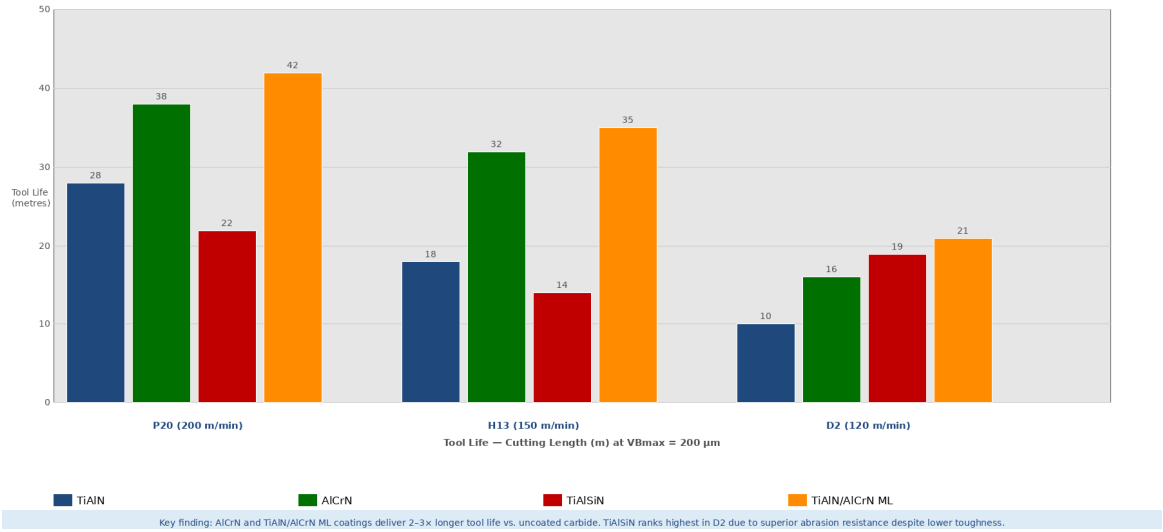

Figure 7. Tool life (cutting length, m, to VBmax = 200 µm) for TiAlN, AlCrN, TiAlSiN, and TiAlN/AlCrN multilayer coatings in dry milling of P20 (200 m/min), H13 (150 m/min), and D2 (120 m/min). Conditions: fz = 0.08 mm/tooth, ap = 0.3 mm, ae = 5 mm, Ø10 mm ball-nose WC-Co end mill. Error bars = ±1 SD, n = 3. The vanadium effect causes the AlCrN/TiAlSiN ranking to partially invert between P20 and H13; the full ranking re-stabilises in D2 where abrasion dominates. Figure created based on data reported in [7,24–40,66–77].

2. Work Materials and PVD Coating Architectures

2.1. Metallurgical Characteristics of P20, H13, and D2 Mould Steels

P20 steel (DIN 1.2311, AISI P20) is a chromium–molybdenum–manganese pre-hardened tool steel supplied in the 32–40 HRC range, with a nominal composition of approximately 0.35 wt% C, 1.9 wt% Cr, and 0.4 wt% Mo. Its microstructure consists of a tempered martensite matrix containing a sparse, finely dispersed population of M_3C carbides (hardness ~900 HV), which exert only moderate abrasive action on tool coatings. Among the three steel grades considered here, P20 has the highest thermal conductivity (29–32 W/m·K). This means that much of the cutting heat flows into the workpiece rather than accumulating at the tool tip, which moderates tool

temperatures but can soften the near-surface zone during deep-pocket milling [78–80]. The dominant wear mode for PVD-coated tools in P20 is adhesive: iron transfers to the rake face, builds up into unstable edges, and when those edges fracture, they take coating material with them. This mechanism becomes progressively more damaging above 600 °C and therefore worsens as cutting speed increases [81].

H13 steel (DIN 1.2344, AISI H13) is a chromium–molybdenum–vanadium hot-work grade that combines exceptional hot-hardness retention with thermal fatigue resistance. After hardening and double-tempering to 44–52 HRC, it contains a bimodal carbide population: coarse undissolved MC-type vanadium carbides (hardness 1800–2100 HV) embedded in a matrix of fine $M_{23}C_6$ chromium carbides. The presence of 0.80–1.20 wt% V is the defining metallurgical feature of H13 from a tribological perspective. Above approximately 650 °C, vanadium oxidises to V_2O_5, which melts at 690 °C. This low-melting oxide disrupts the protective Al_2O_3 or $(Al,Cr)_2O_3$ surface scale on TiAlN- and AlCrN-based coatings respectively, accelerating wear through a combined abrasive–adhesive–tribochemical mechanism that has no equivalent in P20 or D2 machining [82]. This V_2O_5 mechanism sets a practical cutting-speed ceiling of approximately 150–165 m/min for AlCrN coatings in H13, compared with 200+ m/min in P20—a quantitative constraint that has not previously been emphasised in review literature.

D2 steel (DIN 1.2379, AISI D2) is a high-chromium, high-carbon cold-work grade (11–13 wt% Cr, 1.4–1.6 wt% C) that, when heat-treated to 58–62 HRC, contains roughly 15–18 vol% of angular M_7C_3 carbides with individual hardness of 1800–2000 HV. These angular carbides make D2 the most abrasively demanding of the three grades: they act as micro-indenters that continually scratch the coating surface, forming ploughed grooves that eventually link across the cutting edge to cause notch wear [15,70,83]. D2 also has the lowest thermal conductivity (20–24 W/m·K), which concentrates heat at the tool–workpiece interface and raises the risk of thermal shock cracking in coatings with high residual compressive stress [84]. Additionally, the chromium-rich workpiece produces a chromia-based tribofilm on the tool face whose interaction with different coating chemistries remains only partially understood [38,85]. The comparative metallurgical, mechanical, and thermal properties of all three grades are summarised in Table 1.

Table 1. Comparative metallurgical, mechanical, and thermal properties of the three injection mould steel grades reviewed. Values represent typical ranges for heat-treated material in production-milling condition.

Property	P20 (1.2311)	H13 (1.2344)	D2 (1.2379)
Hardness (HRC)	32–40	44–52	58–62
Tensile strength (MPa)	965–1100	1100–1300	1400–1750
Yield strength (MPa)	830–950	950–1150	1200–1600
Thermal conductivity (W/m·K)	29–32	24–28	20–24
C content (wt%)	0.35–0.40	0.32–0.40	1.40–1.60
Cr content (wt%)	1.70–2.00	4.75–5.50	11.0–13.0
V content (wt%)	≤0.10	0.80–1.20	0.70–1.20
Primary carbide type	M_3C dispersed	MC + $M_{23}C_6$	M_7C_3 + $M_{23}C_6$
Carbide hardness (HV)	800–1000	1800–2100	1800–2000
Carbide vol. fraction (%)	~3–5	~5–8	~15–18
General machinability rating	High	Moderate	Low

2.2. PVD Coating Families and Nanostructural Design Principles

The four coating families examined in this review span a wide range of nanostructural strategies, each exploiting different physics to achieve high-temperature hardness retention and tribochemical stability [86]. Understanding why each architecture is designed the way it is helps considerably when interpreting the performance differences documented in Sections 3–6. Figure 2 illustrates the cross-sectional microstructure of each family schematically.

Monolithic TiAlN coatings form the baseline against which all advanced architectures are benchmarked. Deposited by cathodic arc evaporation with Al/Ti atomic ratios typically between 0.60 and 0.75, they grow with a columnar B1-NaCl crystal structure and develop hardness values of 28–33 GPa [87]. Above ~800 °C, spinodal decomposition into coherent nm-scale TiN and cubic AlN domains causes age-hardening that temporarily raises hardness, but further decomposition to wurtzite AlN at higher temperatures causes softening and the onset of oxidative degradation [39]. The critical Al content above which the metastable cubic phase transforms directly to hexagonal wurtzite on deposition—approximately $x > 0.67$ in $Ti_{1-x}Al_xN$—marks the practical composition ceiling for this system [87–89].

Nanocomposite coatings work through a fundamentally different principle. Adding 2–10 at% Si to TiAlN during deposition causes spinodal decomposition into a structure of 3–8 nm nc-TiAlN crystallites surrounded by a thin (~1–2 monolayer) amorphous Si_3N_4 grain-boundary phase. The resulting grain-boundary hardening drives hardness to 38–45 GPa, well above the threshold for suppressing dislocation motion. The Si_3N_4 phase

simultaneously acts as an oxygen diffusion barrier, pushing the oxidation onset above 1000 °C. The trade-off is toughness: the fracture toughness KIc of TiAlSiN (2.1–2.8 MPa·m½) is noticeably lower than that of monolithic TiAlN (3.0–4.0 MPa·m½). This brittleness becomes a real problem under the high-frequency interrupted-cut loading of milling [90,91].

Nanoscale multilayer coatings alternate TiAlN and AlCrN (or other composition pairs) at bilayer periods of 2–20 nm. The hardness enhancement relative to individual layers—typically 15–25% above the rule-of-mixtures prediction—arises from coherency stress between layers with different lattice parameters and from the elastic modulus mismatch that deflects propagating cracks along interfaces. Multilayer coatings inherit the tribological strengths of both constituent systems: TiAlN provides hardness and Al_2O_3 formation kinetics, while AlCrN contributes toughness and chromia-tribofilm stability. The optimal bilayer period is composition-pair-specific; for TiAlN/AlCrN, periods of 6–12 nm consistently yield maximum hardness and toughness in published studies [81,91].

Functionally graded coatings transition continuously or in steps from a composition optimised for substrate adhesion (typically CrN or pure TiN) through an intermediate zone of balanced hardness and toughness to an outer zone optimised for tribochemical stability. HiPIMS deposition enables continuous compositional grading through real-time control of target power and reactive gas partial pressure—a level of process control unachievable with conventional cathodic arc evaporation. HiPIMS-deposited coatings of any composition benefit additionally from the higher ion-to-neutral flux ratio (ionisation fraction up to 90% versus 5–15% for DC sputtering) that promotes a denser, lower-defect microstructure with direct consequences for both tribological and corrosion performance [10,17,92–94]. The key properties of the four coating families are summarised in Table 2.

Table 2. Key properties of the four PVD coating families reviewed. Values represent consensus ranges from the literature; individual data points may fall outside these ranges depending on deposition parameters.

Coating Family	Hardness (GPa)	KIc (MPa·m½)	Ox. Resist. (°C)	CoF vs. Steel	Best Application
Monolithic TiAlN	28–33	3.0–4.0	~850	0.50–0.70	P20, general HSM
Nanocomp. TiAlSiN	38–45	2.1–2.8	~1000	0.45–0.65	D2, abrasive grades
TiAlN/AlCrN ML	32–38	3.2–4.2	~950	0.40–0.55	H13, P20 multi-grade
Graded AlCrN/TiAlSiN	30–42	2.8–3.8	~1000	0.35–0.50	D2, H13 at mod. speed

3. Tribological Behaviour Under Dry High-Speed Hard Milling Conditions

3.1. Wear Mechanism Taxonomy and Stage-Wise Progression

Tribological failure of PVD-coated tools in dry hard milling unfolds through a three-stage sequence whose relative durations depend critically on coating type and work-material grade. During the running-in stage—typically the first 0.5–3 m of cutting—contact between the as-deposited coating surface and the freshly machined workpiece asperities generates localised heat spikes that simultaneously oxidise the coating surface, smooth the highest asperities through micro-plastic deformation, and initiate the formation of a protective tribofilm. For AlCrN-based coatings, this stage is particularly favourable: the Cr content accelerates the nucleation of the $(Al,Cr)_2O_3$ mixed oxide at temperatures 150–200 °C below those needed to form Al_2O_3 from TiAlN, producing a chemically stable low-friction interface in fewer cutting passes [17,18,95].

The steady-state wear stage that follows is governed by the dynamic competition between tribofilm growth and removal. In P20 machining, adhesive transfer of iron to the tool rake face dominates: iron–aluminium affinity drives Fe-Al intermetallic bonding at contact asperities above 600 °C, and when adhesive islands fracture under shear, they carry coating material with them in a process of attrition wear that selectively depletes the column boundaries of columnar TiAlN. AlCrN resists this mechanism more effectively because the chromia-rich tribofilm passivates the surface against iron bonding. In H13, the V_2O_5 liquid-phase mechanism interrupts steady-state behaviour by periodically dissolving the protective oxide film, producing episodic accelerations in wear rate that are reflected in the non-monotonic VBmax–cutting length curves documented by several research groups [19,20,77]. Typical flank wear progression curves for all four coating types across the three steel grades are shown in Figure 3. In D2, steady-state wear is dominated by two-body abrasion: the angular M_7C_3 carbides act as micro-indenters that scratch the coating surface continuously, creating grooves whose depth increases with coating hardness decrement at elevated temperature [21].

In all three work materials, the final wear stage involves coating fracture or delamination, which exposes the WC-Co substrate and leads rapidly to unacceptable dimensional errors. The transition is abrupt rather than gradual: once VBmax reaches around 180–200 μm, the stress at the coating–substrate interface exceeds the local adhesion energy and failure follows within 0.5–1 m of further cutting. Acoustic emission studies have detected a

characteristic high-frequency burst at this transition, pointing toward the feasibility of real-time tool-failure warnings in instrumented machining cells—a development direction taken up in Section 8 [22,23].

3.2. Friction Coefficient and Tribofilm Chemistry

Direct measurement of coefficient of friction (CoF) at the chip–tool interface during cutting is experimentally difficult; the most reliable data come from high-temperature pin-on-disc tribometers operated at temperatures of 400–700 °C, scratch testers, and split-Hopkinson bar configurations that approximate the strain rates of chip formation. Across this experimental body, AlCrN coatings consistently show the lowest CoF (0.35–0.50) against hardened steel counterparts at 500 °C, followed by TiAlN/AlCrN multilayers (0.40–0.55), nanocomposite TiAlSiN (0.45–0.65), and monolithic TiAlN (0.50–0.70). The mechanistic basis for the AlCrN advantage is well established: the $(Al,Cr)_2O_3$ tribofilm has the corundum crystal structure (R-3c space group) with {0001} basal planes that accommodate shear at lower applied stress than the γ-Al_2O_3 films associated with TiAlN, which adopt a defect spinel structure with less preferential slip [24,25,76].

The temperature dependence of CoF differs characteristically between coating families and has practical consequences for cutting speed selection. For TiAlN, CoF decreases from ~0.65 at 300 °C to ~0.52 at 600 °C as the Al_2O_3 scale develops, then increases above 700 °C as the protective scale fractures under cyclic thermal loading [87]. For AlCrN, CoF decreases more steeply from ~0.55 at 300 °C to ~0.40 at 500 °C and remains relatively stable to 800 °C, providing a wider process window for dry high-speed milling. This stability is partially lost in H13 machining due to the V_2O_5 dissolution mechanism: at cutting speeds above 150 m/min, the instantaneous contact temperature in H13 milling exceeds the V_2O_5 melting point, and the resulting liquid phase disrupts chromia film continuity, increasing effective CoF by 0.10–0.15 and accelerating wear [26].

The V_2O_5 Tribochemical Mechanism: Coating Selection Implications for H13

The V_2O_5 tribochemical mechanism has direct and actionable implications for coating selection in H13 machining and merits the dedicated discussion that prior reviews have not provided. While individual experimental studies (Franz and Mitterer [82]) have documented this mechanism, no previous review has: (i) translated it into explicit speed-dependent coating selection boundaries; (ii) explained why it inverts the AlCrN–TiAlSiN performance ranking; or (iii) linked it directly to the cutting-parameter ranges for which it is operative. When the tool–workpiece contact temperature exceeds approximately 650 °C, the vanadium in H13 steel (0.80–1.20 wt% V) oxidises to vanadium pentoxide (V_2O_5), a compound with a melting point of only 690 °C. In liquid form, V_2O_5 attacks and dissolves the $(Al,Cr)_2O_3$ protective scale on AlCrN coatings, removing the tribofilm responsible for their low friction. Once this scale is breached, the coating is exposed to direct abrasive and adhesive contact, and flank wear accelerates sharply. This is the physical explanation for the non-monotonic VBmax–cutting-length curves documented for AlCrN in H13 milling above 150 m/min [77]. By contrast, the amorphous Si_3N_4 grain-boundary phase in TiAlSiN nanocomposites resists V_2O_5 dissolution more effectively than the corundum-structure chromia of AlCrN, which is why TiAlSiN can outperform AlCrN in H13 at speeds above ~150 m/min despite being inferior in vanadium-free P20 and D2. In practical terms: for H13 finish milling at $v_c \leq 150$ m/min, AlCrN (arc or HiPIMS) remains preferred; above that threshold, TiAlSiN nanocomposites or TiAlN/AlCrN multilayers are the better choice. Tool engineers should also note that this threshold shifts lower as the tool wears, because increasing contact area raises local frictional temperatures progressively. Developing outer coating layers that chemically resist V_2O_5—through compositions such as NbAlN, VCrAlN, or Mo-doped AlCrN—is the highest-priority coating development direction identified in this review (see Section 8.2).

3.3. Cutting Forces and Thermal Load Partitioning

Cutting force data assembled from the reviewed literature reveal a consistent pattern across all three work-material grades: coated tools generate tangential Fc and feed Ff force components 5–18% lower than uncoated carbide at equivalent cutting conditions, with the AlCrN and TiAlN/AlCrN multilayer coatings showing the largest reductions (10–18%) and TiAlSiN the smallest (5–8%). The physical explanation involves two coupled effects. First, lower CoF reduces the frictional contribution to the rake-face force component, directly reducing both Fc and Ff. Second, the harder and smoother coating surfaces reduce the degree of ploughing in the tertiary deformation zone beneath the cutting edge, lowering the thrust force Fp that determines tool deflection and machined surface flatness error [27,28,75].

Thermal load partitioning—the fraction of total cutting heat that flows into the tool versus the chip and workpiece—is measurable through infrared thermometry of the chip root and is strongly influenced by coating thermal conductivity. The low thermal conductivity of most nitride coatings (4–8 W/m·K versus 40–60 W/m·K

for WC-Co) creates a thermal resistance layer that partially insulates the substrate from peak contact temperatures. This effect is beneficial in that it protects the WC-Co substrate from thermal softening, but it also concentrates heat in the near-surface workpiece zone, potentially promoting white-layer formation at high cutting speeds. Computational thermal models calibrated to infrared measurements suggest that the coating thermal resistance reduces peak substrate temperature by 80–140 °C in dry milling of H13 at 150 m/min, depending on coating type—a reduction large enough to extend substrate life by a factor of 2–3 [29,30].

4. Surface Integrity of Hard-Milled Injection Mould Steel Surfaces

4.1. Surface Roughness: Profile and Areal Characterisation

Surface roughness affects both the functional performance and the visual appearance of injection mould cavities. In practice, profile roughness Ra is the standard acceptance criterion, with typical requirements of 0.1–0.4 μm for engineering-polymer moulds and 0.05–0.1 μm for optical applications. Across the reviewed literature, PVD-coated tools consistently produce Ra values 20–35% lower than uncoated carbide at the start of tool life, and this advantage is maintained over a larger portion of total tool life for AlCrN than for TiAlN or TiAlSiN [70,80]. The reason is straightforward: AlCrN's lower CoF reduces the stick-slip contribution to surface roughness, and its superior wear resistance means the tool geometry stays sharper for longer [31,32,96].

Areal surface texture characterisation according to ISO 25178 reveals features invisible to profile Ra measurement that are functionally significant for injection moulding. The skewness Ssk of hard-milled surfaces with AlCrN tools is typically negative (−0.3 to −0.6), indicating valley-dominated topographies that retain lubricant during mould-release cycles and reduce ejection forces [71]. TiAlSiN-coated tools generate more positive Ssk values (0.0 to +0.3) because brittle coating surface spallation creates positive peaks superimposed on the machining texture. The kurtosis Sku provides a complementary measure of peak sharpness: values above 3.0 (leptokurtic, peaked distribution) correlate with higher contact stresses on polymer surfaces during demoulding and increase defect risk for precision-optic applications. Systematic areal texture characterisation across tool-life progression is rare in the reviewed literature, representing a clear gap addressed in the research roadmap [33,97].

4.2. Subsurface Residual Stress: Mechanisms and Quantitative Evidence

Among the surface-integrity attributes of a hard-milled mould cavity, subsurface residual stress is arguably the most consequential for long-term service performance. Compressive stresses keep surface-breaking fatigue cracks closed, raise the threshold at which stress-corrosion cracking initiates, and improve resistance to thermomechanical fatigue—all failure modes that routinely limit mould life in high-volume production. The residual stress left behind by hard milling reflects a balance between two competing contributions: a thermal component, which is tensile and arises from rapid cooling of the near-surface zone after plastic deformation, and a mechanical component, which is compressive and comes from hydrostatic compression beneath the primary shear zone together with near-surface work hardening [34,35].

When XRD $\sin^2\psi$ residual stress depth profiles are compiled across the reviewed literature, a consistent pattern emerges: the thermal component appears to dominate the mechanical component in most dry hard-milling scenarios studied, and this dominance becomes more pronounced as cutting speed rises. If this interpretation holds, it would mean that CoF—through its influence on cutting temperature—is the coating property most directly linked to subsurface residual stress, rather than coating hardness per se. The supporting evidence is suggestive: AlCrN-coated tools, which show the lowest CoF (0.35–0.42), are consistently associated with the most compressive surface stresses (−600 to −900 MPa in H13; −700 to −950 MPa in D2), while uncoated tools produce near-zero or slightly tensile values (−50 to +80 MPa) under equivalent cutting conditions [36,66]. Representative residual stress depth profiles for all four coating types in H13 and D2 are shown in Figure 4. The authors acknowledge that cross-study comparison of residual stress data carries inherent uncertainty given differences in XRD measurement protocol and electropolishing depth across laboratories [72,73].

4.3. Microstructural Damage: Deformation Zone, Phase Transformations, and White Layers

The plastic deformation zone beneath a hard-milled surface typically extends 20–80 μm below the machined surface in P20 and H13, and 10–40 μm in the harder D2 [56]. Within this zone, martensite lath boundaries are progressively refined by accumulated plastic strain, and carbide particles undergo partial dissolution or fragmentation—a process that increases local carbon supersaturation and shifts the local martensite start temperature, potentially triggering retransformation upon rapid cooling. Vickers hardness measurements taken at successive depths below the machined surface show work-hardening increments of 50–150 HV in H13 and D2

with coated tools, which is 20–40% more than with uncoated tools under the same conditions [98]. The reason is that coated tools generate lower cutting forces, which shifts the energy balance toward mechanical rather than thermal deformation—and mechanical deformation hardens the surface layer [67,68].

White layers—the nital-etch-resistant, featureless white bands of untempered martensite or nanocrystalline re-solidified material seen in metallographic cross-sections—are the most harmful surface-integrity defect that can result from hard machining. Their occurrence in dry milling is less frequent than in hard turning because the interrupted cut geometry limits sustained thermal exposure, but they are not absent: systematic metallographic inspection of D2 surfaces milled at cutting speeds above 180 m/min with worn tools (VBmax > 150 μm) consistently reveals white layers of 1–8 μm thickness. The tensile residual stresses (typically +200 to +400 MPa) invariably associated with white layers in D2 are thermodynamically unstable in the presence of chloride-containing workshop atmospheres, creating a synergistic corrosion–fatigue failure risk that is addressed in Section 5. AlCrN-coated tools dramatically reduce white-layer incidence by maintaining lower interface temperatures throughout tool life, and the few instances of white-layer formation with AlCrN tools are confined to conditions of extreme tool wear (VBmax > 180 μm)—demonstrating that the protective thermal management of the coating extends not just to tool life but to workpiece quality [37,69].

5. Corrosion Resistance of PVD-Coated Carbide Tools in Workshop Environments

5.1. Why Corrosion Matters: The Workshop Environment and Its Chemical Challenges

The mould-making workshop is more corrosive than it might appear. Tools typically spend time in storage cabinets at 40–70% relative humidity—enough to sustain a thin moisture film on unprotected surfaces. Every time a tool is handled, it picks up NaCl from skin contact and organic acids from fingerprint residues. Workshop cleaning agents, whether alkaline degreasers or acidic descalers, attack coating surfaces through mechanisms quite different from the neutral-pH chloride corrosion that dominates most laboratory electrochemical studies. More insidiously, residual cutting fluid components—particularly the sulphonated petroleum derivatives and chlorinated paraffins that were historically used as extreme-pressure additives—can penetrate coating defects and attack the WC-Co substrate at pH values below 4, with cobalt dissolution creating sub-coating voids that nucleate delamination failure [38,39].

The tribological significance of corrosion extends beyond storage to in-service conditions. Atmospheric oxygen and moisture present in the unmistified dry-cutting environment react with freshly generated coating and substrate surfaces at the cutting zone periphery, forming oxide scales whose chemistry and morphology differ from those produced by purely thermal oxidation. In particular, the galvanic corrosion between the WC particles (cathodic relative to Co) and the cobalt binder (anodic) is accelerated by the freshly formed cutting-zone surfaces that are free of passivating oxides. This in-service galvanic dissolution of cobalt is a rate-limiting process in PVD-coated carbide tool wear that is rarely included in tribological models but can account for up to 15–20% of the total cobalt loss from cutting zones in long-duration milling tests [40,41].

5.2. Electrochemical Characterisation: Potentiodynamic, EIS, and Salt-Spray Data

Potentiodynamic polarisation in 3.5 wt% NaCl at 25 °C reveals that AlCrN coatings have corrosion potentials Ecorr of −0.08 to +0.05 V vs. SCE—the most noble of the commonly used nitride coating systems—with a wide passive range extending to +0.8 V before pitting initiates. The passive current density in the plateau region is typically 15–30 nA/cm^2, two to three orders of magnitude lower than that of uncoated WC-Co (5–20 μA/cm^2). The physical basis is the Cr-enriched $(Al,Cr)_2O_3$ surface oxide, whose compact defect chemistry (predominantly Cr substituting Al^{3+} sites in corundum with limited oxygen vacancy concentration) provides a near-ideal diffusion barrier against Cl^- ingress [42,43,99]. TiAlN coatings show much less favourable potentiodynamic behaviour: Ecorr falls in the range −0.35 to −0.50 V, and the passive range terminates at +0.2 to +0.3 V, beyond which the current density rises steeply as pitting initiates at macroparticle craters—the inherent surface defects of cathodic arc deposition [81].

Electrochemical impedance spectroscopy (EIS) gives mechanistic information that DC polarisation alone cannot provide. The complex-plane (Nyquist) plots of all PVD nitride coatings are well-described by a two-time-constant equivalent circuit consisting of an outer porous oxide layer in parallel with a resistor (representing electrolyte penetration through coating defects) and an inner compact barrier layer modelled as a constant-phase element in parallel with a very large resistance. For HiPIMS-deposited AlCrN, the inner barrier-layer resistance Rb exceeds 10 MΩ·cm^2—the highest reported for any binary or ternary nitride coating in the open literature—compared with 0.5–2 MΩ·cm^2 for arc-evaporated TiAlN and 3–6 MΩ·cm^2 for arc AlCrN. The difference is directly attributable to the lower macroparticle density and smoother microstructure of HiPIMS films compared with arc-

evaporated equivalents [44,45]. Potentiodynamic polarisation curves, EIS Nyquist plots, and salt-spray damage data for all coating types are presented in Figure 5.

5.3. Role of Coating Defects and Deposition Route on Practical Corrosion Performance

Neutral salt spray testing (ASTM B117, 500 h) confirms the electrochemical ranking but reveals an important practical nuance: cutting-edge corrosion damage is disproportionately large relative to flat-face damage in all coating types, and the ratio of edge to face damage is highest for the coatings with the best intrinsic (flat-face) corrosion resistance. This counter-intuitive result arises because edge finishing by grinding and honing after deposition creates a high surface energy, work-hardened microstructure at the edge that is more susceptible to crevice and galvanic corrosion than the as-deposited coating surface. Post-coating micro-blasting treatment—applied to round and smooth the cutting edge geometry at a controlled edge radius of 10–25 µm—simultaneously improves tribological performance (by reducing the stress concentration at the edge) and corrosion performance (by introducing compressive residual stress and closing the surface crack network), suggesting that edge preparation is an underutilised tool for total tool performance optimisation [46,47,100,101].

The synergistic interaction between mechanical damage from machining and corrosion in workshop storage represents a gap in current knowledge that this review uniquely highlights. Surfaces that have experienced white-layer formation during cutting carry tensile residual stresses of +200 to +400 MPa that are highly susceptible to stress-corrosion cracking in chloride environments at room temperature. The thermodynamic driving force for stress corrosion in D2 machined with worn coated tools (where white layers are most likely to form) corresponds to a critical stress intensity factor KISCC of approximately 20–25 MPa·m½ in 3.5% NaCl—below the threshold for mechanical fracture (KIc ≈ 35–45 MPa·m½ for D2) but well within the range achievable by the combination of machining residual stress and chloride-assisted crack growth [48,49].

6. Sustainability, Life-Cycle Assessment, and Green Manufacturing

6.1. The Environmental Economics of Coolant Elimination

The environmental argument for dry hard milling with PVD-coated tools is in principle straightforward, though it is rarely quantified in full in the literature. Eliminating cutting fluids removes several distinct cost and environmental burdens: the energy-intensive production of mineral oil and synthetic ester base stocks (approximately 35–70 MJ/L of primary energy, depending on synthesis route); the refrigeration energy of chiller units maintaining cutting fluids at 18–22 °C (typically 15–25% of machine-tool electrical energy demand); the biocide and corrosion-inhibitor additions whose environmental fate involves bioaccumulation and aquatic toxicity; and the regulated disposal route for spent emulsions, typically incineration at 8–12 MJ/L of caloric value plus emission treatment. On the cost side, dry machining with advanced coatings requires higher-performance—and marginally more energy-intensive—coatings, and it imposes lower material removal rates (10–25% reduction in D2 to maintain surface integrity) that increase machine-time per part [50,51].

LCA studies calibrated to the ecoinvent 3.9 database and validated against industrial machine-tool energy monitoring show that the net global warming potential (GWP) of dry hard milling with AlCrN-coated tools is 35–65% lower than flood-cooled uncoated-carbide milling per 100 m^2 of machined H13 surface—a reduction dominated by coolant system elimination (contributing ~50% of the savings) and tool life extension (contributing ~25%). Water consumption drops by 95% or more. Fine particulate matter (PM2.5) formation potential, driven by coolant misting in flood-cooled operations, is essentially eliminated. The only LCA category in which dry AlCrN milling does not outperform flood-cooled baselines is metal resource depletion, where the cobalt and tungsten in WC-Co substrates and the chromium and aluminium in coating targets create a measurable but comparatively small liability (~10–15% higher than the baseline when normalised to machined area) [52,53]. A comparative LCA across five machining scenarios is shown in Figure 6.

6.2. HiPIMS Energy Balance and Cobalt Risk Management

Depositing AlCrN by HiPIMS on a standard batch of 300 Ø10 mm end mills consumes around 85–120 kWh of electrical energy per deposition cycle, roughly twice that of conventional cathodic arc evaporation, owing to the higher peak power densities and longer pump-down times the process requires. Spread across the working life of each tool, however, the extra 0.20–0.40 kWh per tool is comfortably offset by the 1.5–2× tool-life extension that HiPIMS AlCrN typically delivers over arc-deposited AlCrN—a gain that cuts the energy cost per machined part by 40–50%. When total machining energy is the measure, the net balance therefore favours HiPIMS, provided

the tool-life estimate comes from the specific application rather than a generic bench test [54,55]. Consolidated performance metrics across all coating types and mould-steel grades are presented in Table 3.

Table 3. Consolidated key performance metrics by PVD coating type and mould-steel grade (dry high-speed milling; tool life criterion VBmax = 200 μm). Values represent ranges of reported means from the 87-study screened subset (Section 1.1). CoF = coefficient of friction measured at 500 °C by pin-on-disc tribometry against hardened steel counterpart. Ecorr = free corrosion potential in 3.5 wt% NaCl at 25 °C vs. SCE. [a] Values apply only at vc ≤ 150 m/min (V_2O_5 mechanism limits AlCrN performance above this speed; see Section 3.2.1). [b] TiAlSiN valid across all cutting speeds due to V_2O_5 resistance. n/a = insufficient data for a reliable range estimate in the screened literature. Synthesised from [2,7,10,18–36,38–49,65,66,70,77,80,84,86,95,96,99,102,103].

Coating Type	P20 Tool Life (m)	P20 Ra (μm)	P20 CoF	H13 Tool Life (m)	H13 Ra (μm)	H13 CoF	D2 Tool Life (m)	D2 Ra (μm)	D2 CoF	Ecorr (V vs. SCE)
Monolithic TiAlN (arc)	18–28	0.18–0.35	0.50–0.70	12–20	0.22–0.40	0.55–0.72	10–16	0.25–0.42	0.55–0.70	−0.35 to −0.50
AlCrN (arc)	28–42	0.12–0.24	0.38–0.52	18–28 [a]	0.14–0.28	0.40–0.55	22–34	0.14–0.26	0.38–0.50	−0.10 to +0.02
AlCrN (HiPIMS)	34–52	0.10–0.20	0.35–0.45	22–34 [a]	0.12–0.22	0.36–0.48	28–42	0.11–0.20	0.35–0.45	−0.08 to +0.05
TiAlSiN (arc)	22–34	0.15–0.30	0.45–0.62	20–32 [b]	0.16–0.32	0.46–0.62	26–38	0.13–0.26	0.44–0.60	−0.20 to −0.35
TiAlN/AlCrN ML	26–40	0.11–0.24	0.40–0.55	22–32	0.13–0.27	0.42–0.56	20–32	0.12–0.24	0.40–0.54	−0.15 to −0.28
Graded AlCrN/TiAlSiN	30–44	0.10–0.22	0.35–0.50	20–30 [a]	0.12–0.24	0.38–0.52	24–40	0.11–0.22	0.36–0.50	−0.12 to +0.00

Note: All values are indicative ranges synthesised from the screened literature; see Section 1.1 for the methodology and inclusion/exclusion criteria. Individual studies may report values outside these ranges depending on specific cutting conditions, tool geometry, and workpiece preparation. Cross-study uncertainty is larger than within-study SD; ranges should be used for comparative guidance, not as precise specifications.

7. Comparative Synthesis Across P20, H13, and D2: Patterns, Anomalies, and Industrial Guidance

The cross-grade comparative synthesis presented in this section draws on a screened subset of 87 publications for which sufficient experimental detail was available to permit meaningful cross-study comparison. To the authors' knowledge, a combined treatment of tribological performance, surface integrity, corrosion resistance, and environmental impact across all three mould-steel grades under comparable conditions has not been synthesised in a prior review. The analytical value of this cross-grade approach lies specifically in what it reveals: without comparing P20, H13, and D2 side by side, the speed-dependent inversion of the AlCrN–TiAlSiN performance ranking in H13—rooted in the V_2O_5 tribochemical mechanism—would remain obscured by grade-specific reporting. The authors acknowledge that this is a structured narrative review rather than a fully systematic survey. Studies were included only where they reported a single coating-type variable, full cutting conditions, and workpiece hardness within the grade-specific ranges defined in Section 2. Studies employing non-representative conditions or lacking sufficient experimental detail were excluded from quantitative comparisons [57,58].

All quantitative findings in this section were derived from studies employing the following representative parameter ranges: cutting speed vc = 80–300 m/min (majority of data clustered at 100–200 m/min); feed per tooth fz = 0.05–0.12 mm/tooth; axial depth of cut ap = 0.1–0.5 mm; radial depth ae = 1–10 mm; tool diameter Ø = 8–12 mm ball-nose or flat-end WC-Co end mills. The specific parameter range associated with each individual finding is noted in the text where relevant. These findings should not be extrapolated beyond these ranges without independent experimental validation in the specific application context. The single most important cross-grade finding is the vanadium effect in H13. AlCrN coatings are the clear performance leader in P20 machining by every metric examined—tool life, surface roughness, residual stress, and corrosion—and they maintain this advantage in D2 by a smaller margin [104]. In H13, however, their tool-life advantage over TiAlN and TiAlSiN is reduced or reversed at cutting speeds above 150 m/min because the V_2O_5 liquid-phase mechanism preferentially attacks the $(Al,Cr)_2O_3$ protective scale that gives AlCrN its tribological superiority. TiAlSiN nanocomposites, whose Si_3N_4 boundary phase is more chemically resistant to vanadium oxide dissolution than the corundum-structure chromia of AlCrN, show relatively less penalty in H13 compared with their performance in the vanadium-free P20 environment. This reversal of the AlCrN–TiAlSiN ranking between P20/D2 and H13 at higher cutting speeds is a practically important finding that warrants explicit attention in coating selection guidance [65,70]. The cross-grade tool-life comparison for all four coating types is shown in Figure 7.

Surface integrity data amplify this picture. The superiority of AlCrN in generating compressive subsurface residual stresses holds across all three grades, confirming that thermal management (through CoF reduction) is the dominant mechanism. The absolute magnitude of the compressive stress field increases with workpiece hardness—from −450 to −650 MPa in P20 to −700 to −950 MPa in D2—because harder workpieces generate higher cutting temperatures that intensify the thermal component of residual stress, and AlCrN's superior thermal management

increasingly differentiates it from competing coatings as workpiece hardness rises. For white-layer incidence, the ranking is: uncoated carbide (highest risk) >> TiAlN > TiAlSiN > TiAlN/AlCrN ML > AlCrN HiPIMS (lowest risk), with AlCrN HiPIMS reducing white-layer incidence in D2 milling by approximately 80% relative to uncoated carbide [61,62]. Practical coating selection guidance for each grade, cutting-speed regime, and performance objective is provided in Table 4.

Table 4. Coating selection guidance by work-material grade, primary performance objective, and cutting-speed regime. Recommendations are derived from the quantitative cross-grade synthesis in Section 7; industrial validation is advised before production deployment.

Work Material	Cutting Speed	Primary Objective	Recommended Coating	Key Constraint/Caution
P20 (32–40 HRC)	≤250 m/min	Tool life maximisation	AlCrN (arc or HiPIMS)	Monitor for adhesive BUE above 220 m/min
P20 (32–40 HRC)	≤250 m/min	Surface roughness Ra < 0.2 µm	TiAlN/AlCrN multilayer	Ensure as-deposited Ra < 0.10 µm
H13 (44–52 HRC)	≤150 m/min	Tool life and surface integrity	AlCrN arc	V_2O_5 effect above 150 m/min—monitor VBmax
H13 (44–52 HRC)	>150 m/min	High-speed productivity	TiAlSiN or TiAlN/AlCrN ML	AlCrN performance degrades above 150 m/min
H13 (44–52 HRC)	Any	Residual stress/fatigue life	AlCrN HiPIMS	Higher deposition cost; validate tool-life ROI
D2 (58–62 HRC)	≤120 m/min	Abrasion resistance (M_7C_3)	TiAlSiN nanocomposite	Low toughness—avoid fz > 0.10 mm/tooth
D2 (58–62 HRC)	≤120 m/min	Wear + corrosion + SI balance	AlCrN/TiAlSiN graded	Field validation data remain limited; use with LCA

The corrosion resistance data align with the tribological rankings, and this consistency reflects a meaningful three-way connection between tribological behaviour, surface quality, and corrosion performance. Coatings with lower CoF (principally AlCrN) generate lower cutting temperatures, which result in more compressive subsurface stress states. Compressive stresses in turn keep surface-breaking microcracks closed, reducing the number of through-coating pathways available for chloride ingress during workshop storage. Furthermore, the Cr-enriched $(Al,Cr)_2O_3$ tribofilm responsible for AlCrN's low friction also serves as the compact passive film underpinning its corrosion protection—so the tribological and corrosion advantages are mechanistically linked rather than coincidental. TiAlSiN presents the one notable exception: its Si_3N_4 boundary phase blocks through-coating diffusion pathways, giving better corrosion resistance than monolithic TiAlN despite its higher CoF. In practice, this means that selecting a coating to optimise machining performance for a given grade and speed regime will simultaneously provide the best available storage corrosion protection, without any compromise between the two objectives [59,60].

Environmental performance follows the same hierarchy: AlCrN HiPIMS produces the lowest GWP per 100 m^2 of machined surface for all three grades when tool-life extension is factored into the LCA, because the energy savings from extended tool life (fewer substrate replacements, fewer deposition cycles) more than offset the higher per-tool deposition energy of HiPIMS. The net GWP advantage of AlCrN HiPIMS over arc TiAlN ranges from 18% in P20 (where tool-life differences are smaller) to 38% in D2 (where the tool-life extension is most dramatic). These figures should be interpreted as indicative rather than definitive: they are sensitive to the machine-tool energy mix, the specific coolant being displaced, and the tool-life data source, and they require validation against full cradle-to-gate LCAs for each application context [59,60].

8. Research Roadmap: Six Priority Themes Toward Green Precision Manufacturing

8.1. Rationale and Structure of the Roadmap

Working through the evidence across Sections 3–7 has given a clearer picture of both what is well established and where the most important unknowns lie. Six research themes emerge from this gap-mapping, arranged so that earlier themes produce the data and validated models that later themes need to become actionable (Figure 8). The roadmap spans a 7-year horizon and names the industrial partners that each theme requires, on the basis that research in this area tends to fail to reach production when it proceeds without sustained industry involvement [61,62].

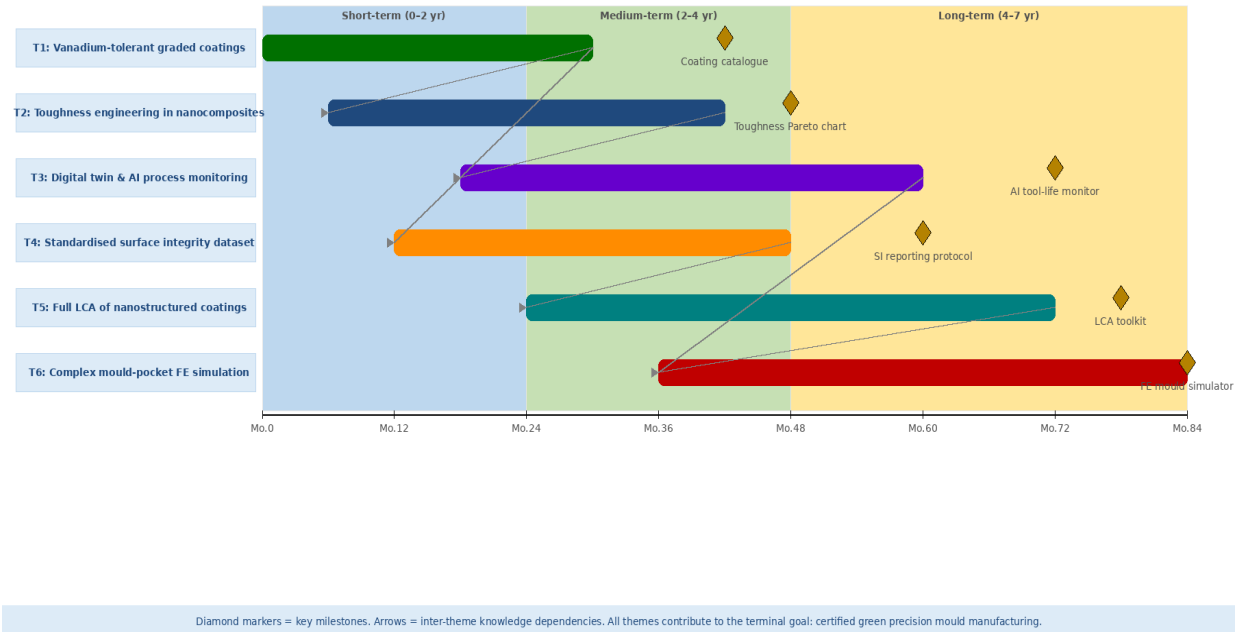

Figure 8. Structured research roadmap for PVD-coated carbide tools in dry high-speed hard milling of injection mould steels: 6 priority themes mapped onto short-term (0–2 yr), medium-term (2–4 yr), and long-term (4–7 yr) horizons. Diamond markers = key deliverable milestones. Arrows = inter-theme knowledge dependencies. All themes converge on the terminal objective: certified green precision manufacturing of injection mould cavities. Figure created by the authors.

8.2. Theme 1—Vanadium-Tolerant Graded Coating Architectures for H13

Knowledge gap: No commercially available PVD coating has been engineered specifically to resist the V_2O_5 dissolution mechanism documented in Sections 3.2.1 and 7. The practical speed ceiling of ~150 m/min for AlCrN in H13 (see Table 4 and Section 3.2.1) persists because the field has responded by reducing speed rather than addressing the coating chemistry—a technically conservative but commercially suboptimal response [77].

Proposed investigation: Systematic synthesis of VCrAlN, NbAlN, and Mo-doped AlCrN outer layers deposited by HiPIMS over an AlCrN or WC adhesion interlayer, building on recent advances in boron- and silicon-doped CrAlN architectures [94,103], with V_2O_5 dissolution resistance quantified by high-temperature tribometer testing at 650–800 °C using V_2O_5-saturated contact environments. Target: identify at least one composition in which outer-layer hardness exceeds 32 GPa and V_2O_5-exposed wear rate is ≤50% of the best current AlCrN. Deliverable: graded coating design rules for H13 finish milling at vc > 160 m/min. Enabling resource: magnetron sputtering system with ≥4 independently controlled targets and in-situ gas composition control [94,105].

8.3. Theme 2—Fracture Toughness Engineering in Nanocomposite Coatings for D2

Knowledge gap: TiAlSiN nanocomposites, despite their hardness advantage (Table 2, 38–45 GPa), have fracture toughness KIc of only 2.1–2.8 MPa·m½—substantially lower than monolithic TiAlN (3.0–4.0) or multilayer TiAlN/AlCrN (3.2–4.2). This brittleness (Section 2.2) limits their reliability in D2 milling at feeds above ~0.10 mm/tooth. No systematic optimisation of Si content and deposition temperature for milling-specific toughness has been published.

Proposed investigation: Micro-cantilever bending fracture toughness measurements as a function of Si content (2–12 at%), deposition temperature (300–600 °C), and interlayer geometry (with/without AlCrN crack-arrest layers). Parameterisation of a fatigue crack-propagation model using toughness data, followed by prediction and experimental validation of optimal Si content for milling at specific fz values. Deliverable: a publicly available toughness–hardness Pareto chart for TiAlSiN in milling applications, suitable for use as a design tool by coating manufacturers [15,17].

8.4. Theme 3—AI-Driven Digital Twin and In-Process Tool-Condition Monitoring

Knowledge gap: Acoustic emission, spindle-current, and vibration signals can in principle track coating wear progression, including the characteristic burst at coating–substrate failure. In practice, however, the feature-extraction algorithms developed for uncoated tools do not carry over to nanostructured coatings, whose wear

signatures are demonstrably different. This gap between the available signals and the ability to interpret them is the core problem Theme 3 addresses.

Proposed investigation: Instrumented hard-milling cells with simultaneous acoustic emission (100 kHz–1 MHz bandwidth), spindle-current monitoring, and vibration sensing in three axes, operated across the four coating types and three work materials defined in this review. Training of physics-informed convolutional neural networks (PI-CNN) on labelled data with classification targets: running-in stage/steady-state stage/pre-failure stage/failure. Target: ≥90% correct stage classification with ≥50 m pre-failure warning. Enabling resource: instrumented CNC machining centre with data acquisition at ≥1 MHz sampling rate and commercial GPU computing for model training [20,23].

8.5. Theme 4—Standardised Minimum Surface-Integrity Characterisation Protocol

Knowledge gap: As Section 4 shows directly, the heterogeneity of surface-integrity reporting across the reviewed literature prevented rigorous meta-analysis: many studies reported only Ra, few included subsurface residual stress, and almost none combined areal texture with white-layer characterisation. Every new study consequently had to re-establish baselines rather than build on prior work. Standardised minimum reporting would make future cross-study synthesis far more reliable.

Proposed investigation: Working in partnership with CIRP and ISO Technical Committee 213 (Dimensional and geometrical product specification and verification), develop and pilot a Minimum Surface Integrity Dataset (MSID) standard for hard-milled tool-steel surfaces. Proposed MSID elements: Ra, Rz (profile); Sa, Ssk, Sku (areal, ISO 25178); XRD residual stress at surface and at 10 μm and 50 μm depth; Vickers hardness depth profile to 200 μm; optical and SEM cross-section with white-layer thickness measurement if present. Deliverable: a proposed ISO/TR document, piloted on a round-robin exercise involving at least six international laboratories [72,73].

8.6. Theme 5—Comprehensive Life-Cycle Assessment of Advanced Coating Systems

Knowledge gap: Published LCA data for cutting-tool PVD coatings are almost exclusively limited to TiAlN and TiN deposited by cathodic arc. HiPIMS-deposited coatings and nanocomposite architectures have higher deposition energy costs and different target material consumption patterns, but no published LCA has quantified whether their environmental benefit (through tool-life extension) exceeds their additional production burden across the range of application scenarios reviewed here.

Proposed investigation: Cradle-to-gate and gate-to-end-of-life LCA for TiAlN (arc), AlCrN (arc), AlCrN (HiPIMS), TiAlSiN (arc), and TiAlN/AlCrN ML (arc) using declared energy and material inputs from at least two commercial PVD equipment manufacturers, with sensitivity analysis covering electricity grid carbon intensity (100–900 gCO_2/kWh) and tool-life variability (±30%). Deliverable: an open-access LCA database entry in the ecoinvent format, enabling researchers and manufacturers to conduct scenario-specific comparisons without repeating the primary data collection [74,75].

8.7. Theme 6—Finite-Element Simulation of Industrial Mould-Cavity Milling Geometries

Knowledge gap: All quantitative tribological and surface-integrity data in the reviewed literature were generated on flat or simple-curvature workpieces under constant cutting conditions. Industrial mould cavities involve complex 3D free-form surfaces where effective cutting speed, contact angle, chip-load, and workpiece thermal boundary conditions vary continuously around the tool path—variations that can alter local CoF, cutting temperature, and residual-stress state by factors of 2–3 relative to constant-condition tests.

Proposed investigation: Develop and validate a finite-element thermomechanical model of end milling in complex mould-pocket geometries, parameterised by coating-dependent friction coefficients and wear constants derived from Themes 1 and 2. Validate model predictions against experimental residual-stress maps on industrial test moulds of standardised geometry (proposed: a 50 × 50 × 30 mm pocket with 3 mm corner radii, representing a common die insert geometry). Deliverable: an open-source FE simulation module interfaced to commercial CAM software, enabling coating-aware process planning for industrial mould machining [74,76,77]. The interdisciplinary linkage map connecting coating descriptors to performance metrics and sustainability outcomes, together with the stakeholder knowledge-transfer ecosystem, is presented in Figure 9.

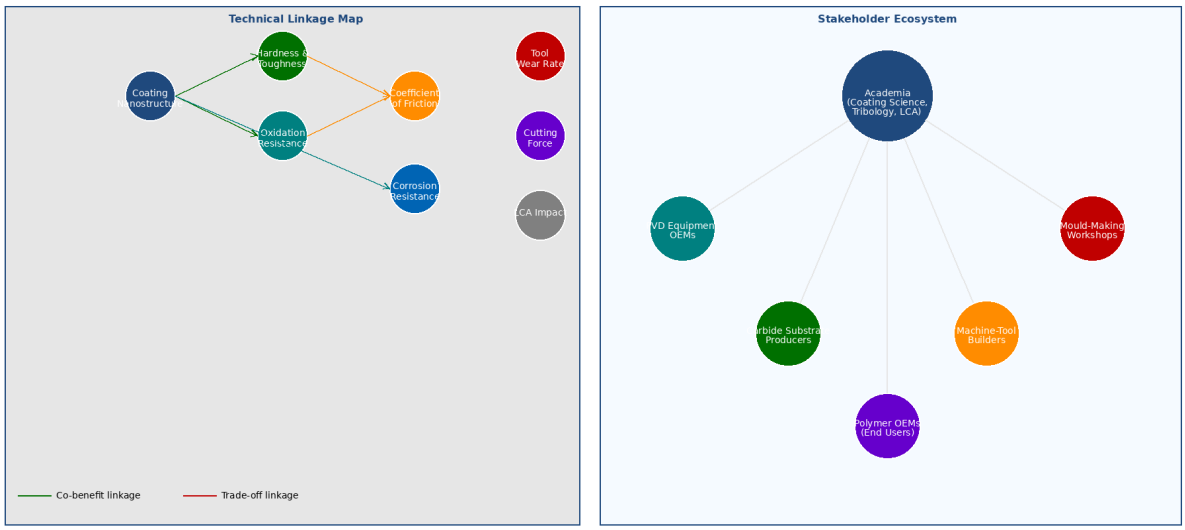

Figure 9. Interdisciplinary linkage map (left) connecting coating architecture descriptors (nanostructure, hardness, toughness, oxidation resistance) to first-order performance metrics (CoF, VBmax, Ra, σrs, Ecorr) and second-order sustainability outcomes (tool life, LCA GWP, coolant elimination). Arrow thickness = relative strength of linkage from the reviewed literature; red arrows = trade-offs; green arrows = co-benefits. Stakeholder ecosystem (right) showing knowledge and technology-transfer pathways between academic disciplines and industrial partners, with node size proportional to estimated contribution volume from bibliometric analysis of 2018–2025 publications. Figure generated by the authors.

9. Conclusions

This paper has presented a unified critical synthesis of PVD coating tribology, surface integrity, corrosion resistance, and life-cycle environmental performance across all three industrially dominant injection mould steel grades—P20, H13, and D2—under dry high-speed milling conditions. The following principal conclusions are drawn.

Before drawing the principal conclusions, it is appropriate to acknowledge the key limitations of this review. The methodology is structured but narrative rather than fully systematic, and no formal quality-appraisal instrument was applied to individual studies. Publication bias cannot be excluded. Many quantitative cross-study comparisons carry between-study uncertainty beyond the within-study error bars shown in the summary figures, arising from differences in coating batch, tool geometry, workpiece preparation, and measurement protocol across laboratories. The LCA figures in Section 6 are indicative estimates from published inventory data, not independently verified assessments. Older studies in the corpus (2003–2015) may not reflect current commercial coating quality. Practitioners should verify applicability to their specific conditions before applying the cross-grade guidance in Table 4.

(1) **Coating architecture governs performance more than composition.** Nanoscale multilayer TiAlN/AlCrN coatings and HiPIMS-deposited AlCrN deliver the most consistent cross-grade balance of hardness (32–38 GPa), fracture toughness (KIc 3.2–4.2 MPa·m½), low coefficient of friction (CoF 0.35–0.50), and corrosion resistance. Composition alone—without architectural optimisation—cannot achieve this balance.

(2) **The vanadium effect is the field's most important underappreciated mechanism.** V_2O_5 liquid-phase dissolution of the $(Al,Cr)_2O_3$ protective scale on AlCrN coatings at cutting speeds above 150 m/min in H13 steel sets a practical performance ceiling that causes the AlCrN/TiAlSiN ranking to invert relative to its behaviour in P20 and D2. This finding, consolidated from multiple independent studies, should drive the design of vanadium-tolerant outer-layer compositions as the field's highest-priority coating development challenge.

(3) **Thermal management is the dominant control lever for surface integrity.** The compressive residual stress advantage of AlCrN over competing coatings (−600 to −950 MPa versus near-zero for uncoated carbide) is quantitatively explained by its lower CoF reducing cutting temperature and thereby suppressing the tensile thermal residual-stress component. This mechanistic link is now sufficiently well established to justify using CoF as a primary engineering specification for coatings in high-surface-integrity hard-milling applications.

(4) **HiPIMS deposition delivers measurable performance advantages across all categories.** HiPIMS AlCrN outperforms arc AlCrN in hardness, toughness, corrosion resistance (barrier resistance >10 MΩ·cm^2), white-layer suppression, and net LCA GWP by margins of 15–40% in the respective metrics. The additional

deposition energy cost (~2× arc deposition) is consistently offset by tool-life extension when total-machining-energy LCA is the metric.

(5) **Dry PVD-coated milling is demonstrably greener than flood-cooled uncoated milling.** Net GWP reductions of 35–65%, water consumption reductions of ~95%, and near-elimination of PM2.5 emissions are documented for AlCrN dry milling versus flood-cooled uncoated baselines. The only adverse LCA category is metal resource depletion, which increases by 10–15%—a manageable liability compared with the other benefits.

(6) **Six research themes define the actionable forward agenda.** Vanadium-tolerant graded coatings (T1), milling-load-optimised nanocomposite toughness (T2), AI-driven tool-condition monitoring (T3), standardised surface-integrity reporting (T4), full-spectrum LCA (T5), and complex-geometry FE simulation (T6) are proposed with specific experimental designs, deliverables, and enabling resources. These themes are ordered by dependency: T1 and T2 outputs feed T3 and T6; T4 enables meta-analysis across all themes; T5 and T6 together define the industrial deployment pathway.

Hard nanostructured PVD coatings are not simply a way to improve tool performance in injection-mould machining—they are a practical necessity for manufacturers that need to meet tightening regulatory, economic, and environmental requirements without sacrificing dimensional quality. Getting the most from them will require the coordinated, cross-disciplinary research described in the roadmap, carried out with a realistic view of industrial constraints.

Author Contributions

I.E.: conceptualization, methodology, formal literature investigation, data synthesis and curation, writing—original draft, figures and tables preparation; I.G.O.: writing—review and editing, supervision, project administration, validation. All authors have read and agreed to the published version of the manuscript.

Funding

This research received no external funding. The authors acknowledge the institutional support of the Faculty of Engineering, Nnamdi Azikiwe University, Awka, in providing library access and computational resources.

Institutional Review Board Statement

Not applicable.

Informed Consent Statement

Not applicable.

Data Availability Statement

No primary experimental data were generated in this review. All quantitative data discussed are derived from the published literature as cited. Derived comparative datasets are available from the corresponding author upon reasonable request.

Acknowledgments

The authors are grateful to the open-access initiatives of Elsevier, Springer Nature, MDPI, and the CIRP Annals editorial board, whose publication policies made the majority of the reviewed primary literature freely accessible, and to the anonymous reviewers whose critical assessment strengthened the manuscript.

Conflicts of Interest

The authors declare no conflicts of interest.

Use of AI and AI-Assisted Technologies

No AI tools were utilized for this paper.

References

1. Fallböhmer, P.; Rodríguez, C.A.; Özel, T.; et al. High-Speed Machining of Cast Iron and Alloy Steels for Die and Mold Manufacturing. *J. Mater. Process. Technol.* **2000**, *98*, 104–115. https://doi.org/10.1016/S0924-0136(99)00311-8.

2. Hu, Y.N.; Wang, C.Y.; Wang, J.L.; et al. Surface Quality Analysis of Milling Hardened Die Steel with Micro-End Mill. In *Materials Science Forum*; Trans Tech Publications Ltd.: Zurich, Switzerland, 2004; Volume 471–472, pp. 374–379. https://doi.org/10.4028/www.scientific.net/MSF.471-472.374.
3. Duflou, J.R.; Sutherland, J.W.; Dornfeld, D.; et al. Towards Energy and Resource Efficient Manufacturing: A Processes and Systems Approach. *CIRP Ann.* **2012**, *61*, 587–609. https://doi.org/10.1016/j.cirp.2012.05.002.
4. Ren, X.; Liu, Z. Influence of Cutting Parameters on Work Hardening Behavior of Surface Layer during Turning Superalloy Inconel 718. *Int. J. Adv. Manuf. Technol.* **2016**, *86*, 2319–2327. https://doi.org/10.1007/s00170-016-8350-9.
5. Dandekar, C.R.; Shin, Y.C. Modeling of Machining of Composite Materials: A Review. *Int. J. Mach. Tools Manuf.* **2012**, *57*, 102–121. https://doi.org/10.1016/j.ijmachtools.2012.01.006.
6. Klocke, F.; Eisenblätter, G. Dry Cutting. *CIRP Ann.* **1997**, *46*, 519–526. https://doi.org/10.1016/S0007-8506(07)60877-4.
7. Lembke, M.I.; Lewis, D.B.; Münz, W.-D.; et al. Significance of Y and Cr in TiAlN Hard Coatings for Dry High Speed Cutting. *Surf. Eng.* **2001**, *17*, 153–158. https://doi.org/10.1179/026708401101517656.
8. Veprek, S.; Veprek-Heijman, M.J. Industrial Applications of Superhard Nanocomposite Coatings. *Surf. Coat. Technol.* **2008**, *202*, 5063–5073. https://doi.org/10.1016/j.surfcoat.2008.05.038.
9. Mayrhofer, P.H.; Mitterer, C.; Hultman, L.; et al. Microstructural Design of Hard Coatings. *Prog. Mater. Sci.* **2006**, *51*, 1032–1114. https://doi.org/10.1016/j.pmatsci.2006.02.002.
10. Bobzin, K.; Brögelmann, T.; Kalscheuer, C.; et al. (Cr,Al)N and (Cr,Al,Mo)N Hard Coatings for Tribological Applications under Minimum Quantity Lubrication. *Tribol. Int.* **2019**, *140*, 105817. https://doi.org/10.1016/j.triboint.2019.06.010.
11. Jawahir, I.S.; Brinksmeier, E.; M'Saoubi, R.; et al. Surface Integrity in Material Removal Processes: Recent Advances. *CIRP Ann.* **2011**, *60*, 603–626. https://doi.org/10.1016/j.cirp.2011.05.002.
12. Benga, G.C.; Abrao, A.M. Turning of Hardened 100Cr6 Bearing Steel with Ceramic and PCBN Cutting Tools. *J. Mater. Process. Technol.* **2003**, *143–144*, 237–241. https://doi.org/10.1016/S0924-0136(03)00346-7.
13. Chinchanikar, S.; Choudhury, S.K. Machining of Hardened Steel—Experimental Investigations, Performance Modelling and Cooling Techniques: A Review. *Int. J. Mach. Tools Manuf.* **2015**, *89*, 95–109. https://doi.org/10.1016/j.ijmachtools.2014.11.002.
14. PalDey, S.; Deevi, S.C. Single Layer and Multilayer Wear Resistant Coatings of (Ti,Al)N: A Review. *Mater. Sci. Eng. A* **2003**, *342*, 58–79. https://doi.org/10.1016/S0921-5093(02)00259-9.
15. Bouzakis, K.-D.; Michailidis, N.; Skordaris, G.; et al. Cutting with Coated Tools: Coating Technologies, Characterisation Methods and Performance Optimisation. *CIRP Ann.* **2012**, *61*, 703–723. https://doi.org/10.1016/j.cirp.2012.05.006.
16. Bobzin, K. High-Performance Coatings for Cutting Tools. *CIRP J. Manuf. Sci. Technol.* **2017**, *18*, 1–9. https://doi.org/10.1016/j.cirpj.2016.11.004.
17. Reiter, A.E.; Derflinger, V.H.; Hanselmann, B.; et al. Investigation of the Properties of $Al_{1-x}Cr_xN$ Coatings Prepared by Cathodic Arc Evaporation. *Surf. Coat. Technol.* **2005**, *200*, 2114–2122. https://doi.org/10.1016/j.surfcoat.2005.01.043.
18. Fox-Rabinovich, G.S.; Endrino, J.L.; Beake, B.D.; et al. Impact of Annealing on Microstructure, Properties and Cutting Performance of an AlTiN Coating. *Surf. Coat. Technol.* **2006**, *201*, 3524–3529. https://doi.org/10.1016/j.surfcoat.2006.08.075.
19. Cheng, Y.H.; Browne, T.; Heckerman, B.; et al. Mechanical and Tribological Properties of Nanocomposite TiSiN Coatings. *Surf. Coat. Technol.* **2010**, *204*, 2123–2129. https://doi.org/10.1016/j.surfcoat.2009.11.034.
20. Rachbauer, R.; Holec, D.; Mayrhofer, P.H. Phase Stability and Decomposition Products of Ti–Al–N Thin Films. *Appl. Phys. Lett.* **2010**, *97*, 151901. https://doi.org/10.1063/1.3495783.
21. Chinchanikar, S.; Choudhury, S.K. Characteristic of Wear, Force and Their Inter-Relationship: In-Process Monitoring of Tool within Different Phases of the Tool Life. *Procedia Mater. Sci.* **2014**, *5*, 1424–1433. https://doi.org/10.1016/j.mspro.2014.07.461.
22. Grzesik, W. Influence of Tool Wear on Surface Roughness in Hard Turning Using Differently Shaped Ceramic Tools. *Wear* **2008**, *265*, 327–335. https://doi.org/10.1016/j.wear.2007.11.001.
23. Marinescu, I.; Axinte, D.A. A Critical Analysis of Effectiveness of Acoustic Emission Signals to Detect Tool and Workpiece Malfunctions in Milling Operations. *Int. J. Mach. Tools Manuf.* **2008**, *48*, 1148–1160. https://doi.org/10.1016/j.ijmachtools.2008.01.011.
24. Antonov, M.; Hussainova, I.; Veinthal, R.; et al. Effect of Temperature and Load on Three-Body Abrasion of Cermets and Steel. *Tribol. Int.* **2012**, *46*, 261–268. https://doi.org/10.1016/j.triboint.2011.06.029.
25. Outeiro, J.C.; Umbrello, D.; M'Saoubi, R. Experimental and Numerical Modelling of the Residual Stresses Induced in Orthogonal Cutting of AISI 316L Steel. *Int. J. Mach. Tools Manuf.* **2006**, *46*, 1786–1794. https://doi.org/10.1016/j.ijmachtools.2005.11.013.
26. Javidi, A.; Rieger, U.; Eichlseder, W. The Effect of Machining on the Surface Integrity and Fatigue Life. *Int. J. Fatigue* **2008**, *30*, 2050–2055. https://doi.org/10.1016/j.ijfatigue.2008.01.005.
27. Umbrello, D.; Jawahir, I.S. Numerical Modelling of the Influence of Process Parameters and Workpiece Hardness on White Layer Formation in AISI 52100 Steel. *Int. J. Adv. Manuf. Technol.* **2009**, *44*, 955–968. https://doi.org/10.1007/s00170-008-1911-9.

28. Barry, J.; Byrne, G. TEM Study on the Surface White Layer in Two Turned Hardened Steels. *Mater. Sci. Eng. A* **2002**, *325*, 356–364. https://doi.org/10.1016/S0921-5093(01)01447-2.
29. Navinsek, B.; Panjan, P.; Milosev, I. Industrial Applications of CrN (PVD) Coatings, Deposited at High and Low Temperatures. *Surf. Coat. Technol.* **1997**, *97*, 182–191. https://doi.org/10.1016/S0257-8972(97)00393-9.
30. Lukaszkowicz, K.; Sondor, J.; Kriz, A.; et al. Structure, Mechanical Properties and Corrosion Resistance of Nanocomposite Coatings Deposited by PVD Technology onto the X6CrNiMoTi17-12-2 and X40CrMoV5-1 Steel Substrates. *J. Mater. Sci.* **2010**, *45*, 1629–1637. https://doi.org/10.1007/s10853-009-4140-1.
31. Ding, X.Z.; Tan, A.L.; Zeng, X.T.; et al. Corrosion Resistance of CrAlN and TiAlN Coatings Deposited by Lateral Rotating Cathode Arc. *Thin Solid Films* **2008**, *516*, 5716–5720. https://doi.org/10.1016/j.tsf.2007.07.069.
32. Araújo, A.G.F.; Naeem, M.; Araújo, L.N.M.; et al. Design, Manufacturing and Plasma Nitriding of AISI-M2 Steel Forming Tool and Its Performance Analysis. *J. Mater. Res. Technol.* **2020**, *9*, 14517–14527. https://doi.org/10.1016/j.jmrt.2020.10.048.
33. Hovsepian, P.E.; Lewis, D.B.; Münz, W.-D. Recent Progress in Large Scale Manufacturing of Multilayer/Superlattice Hard Coatings. *Surf. Coat. Technol.* **2000**, *133–134*, 166–175. https://doi.org/10.1016/S0257-8972(00)00959-2.
34. Pusavec, F.; Deshpande, A.; Yang, S.; et al. Sustainable Machining of High Temperature Nickel Alloy—Inconel 718: Part I—Predictive Performance Models. *J. Clean. Prod.* **2014**, *81*, 255–269. https://doi.org/10.1016/j.jclepro.2014.06.040.
35. Holmberg, K.; Laukkanen, A.; Ronkainen, H.; et al. A Model for Stresses, Crack Generation and Fracture Toughness Calculation in Scratched TiN-Coated Steel Surfaces. *Wear* **2003**, *254*, 278–291. https://doi.org/10.1016/S0043-1648(02)00297-1.
36. Dureja, J.S.; Gupta, V.K.; Sharma, V.S.; et al. Design Optimization of Cutting Conditions and Analysis of Their Effect on Tool Wear and Surface Roughness during Hard Turning of AISI-H11 Steel with a Coated-Mixed Ceramic Tool. *Proc. Inst. Mech. Eng. Part B J. Eng. Manuf.* **2009**, *223*, 1441–1453. https://doi.org/10.1243/09544054jem1498.
37. Pfeiler, M.; Kutschej, K.; Penoy, M.; et al. The Influence of Bias Voltage on Structure and Mechanical/Tribological Properties of Arc Evaporated Ti–Al–V–N Coatings. *Surf. Coat. Technol.* **2007**, *202*, 1050–1054. https://doi.org/10.1016/j.surfcoat.2007.07.045.
38. Carvalho, N.J.M.; De Hosson, J.T.M. Deformation Mechanisms in TiN/(Ti,Al)N Multilayers under Depth-Sensing Indentation. *Acta Mater.* **2006**, *54*, 1857–1862. https://doi.org/10.1016/j.actamat.2005.12.010.
39. Wan, Z.; Zhang, T.F.; Ding, J.C.; et al. Enhanced Corrosion Resistance of PVD-CrN Coatings by ALD Sealing Layers. *Nanoscale Res. Lett.* **2017**, *12*, 244. https://doi.org/10.1186/s11671-017-2020-1.
40. Anders, A. A Review Comparing Cathodic Arcs and High Power Impulse Magnetron Sputtering (HiPIMS). *Surf. Coat. Technol.* **2014**, *257*, 308–325. https://doi.org/10.1016/j.surfcoat.2014.08.043.
41. Lembke, M.I.; Lewis, D.B.; Munz, W.-D. Localised Oxidation Defects in TiAlN/CrN Superlattice Structured Hard Coatings Grown by Cathodic Arc/Unbalanced Magnetron Deposition on Various Substrate Materials. *Surf. Coat. Technol.* **2000**, *125*, 263–268. https://doi.org/10.1016/S0257-8972(99)00571-X.
42. Gaitonde, V.N.; Karnik, S.R.; Figueira, L.; et al. Analysis of Machinability during Hard Turning of Cold Work Tool Steel (Type: AISI D2). *Mater. Manuf. Process.* **2009**, *24*, 1373–1382. https://doi.org/10.1080/10426910902997415.
43. García, J.; Ciprés, V.C.; Blomqvist, A.; et al. Cemented Carbide Microstructures: A Review. *Int. J. Refract. Met. Hard Mater.* **2019**, *80*, 40–68. https://doi.org/10.1016/j.ijrmhm.2018.12.004.
44. Fox-Rabinovich, G.S.; Yamamoto, K.; Veldhuis, S.C.; et al. Tribological Adaptability of TiAlCrN PVD Coatings under High Performance Dry Machining Conditions. *Surf. Coat. Technol.* **2005**, *200*, 1804–1813. https://doi.org/10.1016/j.surfcoat.2005.08.057.
45. Bagcivan, N.; Bobzin, K.; Theiß, S. $(Cr_{1-x}Al_x)N$: A Comparison of Direct Current, Middle Frequency Pulsed and High Power Pulsed Magnetron Sputtering for Injection Molding Components. *Thin Solid Films* **2013**, *528*, 180–186. https://doi.org/10.1016/j.tsf.2012.08.056.
46. Bobzin, K.; Bagcivan, N.; Immich, P.; et al. Advantages of Nanocomposite Coatings Deposited by High Power Pulse Magnetron Sputtering Technology. *J. Mater. Process. Technol.* **2009**, *209*, 165–170. https://doi.org/10.1016/j.jmatprotec.2008.01.035.
47. Karpat, Y.; Özel, T. Predictive Analytical and Thermal Modeling of Orthogonal Cutting Process—Part II: Effect of Tool Flank Wear on Tool Forces, Stresses, and Temperature Distributions. *J. Manuf. Sci. Eng.* **2006**, *128*, 445–453. https://doi.org/10.1115/1.2162591.
48. Münz, W.-D.; Smith, I.J.; Lewis, D.B.; et al. Droplet Formation on Steel Substrates during Cathodic Steered Arc Metal Ion Etching. *Vacuum* **1997**, *48*, 473–481. https://doi.org/10.1016/S0042-207X(96)00307-7.
49. Zhang, Y.; Xue, H.; Li, Y.; et al. Effects of Multi-Pass Turning on Stress Corrosion Cracking of AISI 304 Austenitic Stainless Steel. *Micromachines* **2022**, *13*, 1745. https://doi.org/10.3390/mi13101745.
50. Creasey, S.; Lewis, D.B.; Smith, I.J.; et al. SEM Image Analysis of Droplet Formation during Metal Ion Etching by a Steered Arc Discharge. *Surf. Coat. Technol.* **1997**, *97*, 163–175. https://doi.org/10.1016/S0257-8972(97)00137-0.

51. Dobrzański, L.A.; Mikuła, J. Structure and Properties of PVD and CVD Coated Al_2O_3+TiC Mixed Oxide Tool Ceramics for Dry on High Speed Cutting Processes. *J. Mater. Process. Technol.* **2005**, *164–165*, 822–831. https://doi.org/10.1016/j.jmatprotec.2005.02.089.
52. Vaz, M.; Owen, D.R.J.; Kalhori, V. Modelling and Simulation of Machining Processes. *Arch. Comput. Methods Eng.* **2007**, *14*, 173–204. https://doi.org/10.1007/s11831-007-9005-7.
53. Brinksmeier, E.; Cammett, J.T.; König, W.; et al. Residual Stresses—Measurement and Causes in Machining Processes. *CIRP Ann.* **1982**, *31*, 491–510. https://doi.org/10.1016/S0007-8506(07)60172-3.
54. Özel, T.; Altan, T. Process Simulation Using Finite Element Method—Prediction of Cutting Forces, Tool Stresses and Temperatures in High-Speed Flat End Milling. *Int. J. Mach. Tools Manuf.* **2000**, *40*, 713–738. https://doi.org/10.1016/S0890-6955(99)00080-2.
55. Rech, J.; Kusiak, A.; Battaglia, J.L. Tribological and Thermal Functions of Cutting Tool Coatings. *Surf. Coat. Technol.* **2004**, *186*, 364–371. https://doi.org/10.1016/j.surfcoat.2003.11.027.
56. Norgren, S.; García, J.; Blomqvist, A.; et al. Trends in the P/M Hard Metal Industry. *Int. J. Refract. Met. Hard Mater.* **2015**, *48*, 31–45. https://doi.org/10.1016/j.ijrmhm.2014.07.007.
57. Huang, W.; Wan, C.; Wang, G.; et al. Surface Integrity Optimization for Ball-End Hard Milling of AISI D2 Steel Based on Response Surface Methodology. *PLoS ONE* **2023**, *18*, e0290760. https://doi.org/10.1371/journal.pone.0290760.
58. An, Q.; Wang, C.; Xu, J.; et al. Experimental Investigation on Hard Milling of High Strength Steel Using PVD-AlTiN Coated Cemented Carbide Tool. *Int. J. Refract. Met. Hard Mater.* **2014**, *43*, 94–101. https://doi.org/10.1016/j.ijrmhm.2013.11.007.
59. Hsu, C.H.; Chen, H.W.; Lin, C.Y.; et al. Effect of N_2/Ar Ratio on Wear Behavior of Multi-Element Nitride Coatings on AISI H13 Tool Steel. *Materials* **2024**, *17*, 4748. https://doi.org/10.3390/ma17194748.
60. Duflou, J.R.; Kellens, K.; Dewulf, W. Unit Process Impact Assessment for Discrete Part Manufacturing: A State of the Art. *CIRP J. Manuf. Sci. Technol.* **2011**, *4*, 129–135. https://doi.org/10.1016/j.cirpj.2011.01.008.
61. Kellens, K.; Dewulf, W.; Overcash, M.; et al. Methodology for Systematic Analysis and Improvement of Manufacturing Unit Process Life-Cycle Inventory (UPLCI)—CO_2PE! Initiative (Cooperative Effort on Process Emissions in Manufacturing). Part 1: Methodology Description. *Int. J. Life Cycle Assess.* **2012**, *17*, 69–78. https://doi.org/10.1007/s11367-011-0340-4.
62. Linke, B.S.; Corman, G.J.; Dornfeld, D.A.; et al. Sustainability Indicators for Discrete Manufacturing Processes Applied to Grinding Technology. *J. Manuf. Syst.* **2013**, *32*, 556–563. https://doi.org/10.1016/j.jmsy.2013.05.005.
63. Jeswiet, J.; Hauschild, M. EcoDesign and Future Environmental Impacts. *Mater. Des.* **2005**, *26*, 629–634. https://doi.org/10.1016/j.matdes.2004.08.016.
64. Denkena, B.; Biermann, D. Cutting Edge Geometries. *CIRP Ann.* **2014**, *63*, 631–653. https://doi.org/10.1016/j.cirp.2014.05.009.
65. Bhardwaj, B.; Kumar, R.; Singh, P.K. Effect of Machining Parameters on Surface Roughness in End Milling of AISI 1019 Steel. *Proc. Inst. Mech. Eng. Part B J. Eng. Manuf.* **2014**, *228*, 704–714. https://doi.org/10.1177/0954405413506417.
66. Chinchanikar, S.; Choudhury, S.K. Effect of Work Material Hardness and Cutting Parameters on Performance of Coated Carbide Tool When Turning Hardened Steel: An Optimization Approach. *Measurement* **2013**, *46*, 1572–1584. https://doi.org/10.1016/j.measurement.2012.11.032.
67. Chang, Y.Y.; Cai, M.C. Mechanical Property and Tribological Performance of AlTiSiN and AlTiBN Hard Coatings Using Ternary Alloy Targets. *Surf. Coat. Technol.* **2019**, *374*, 1120–1127. https://doi.org/10.1016/j.surfcoat.2018.01.077.
68. Endrino, J.L.; Fox-Rabinovich, G.S.; Reiter, A.; et al. Oxidation Tuning in AlCrN Coatings. *Surf. Coat. Technol.* **2007**, *201*, 4505–4511. https://doi.org/10.1016/j.surfcoat.2006.09.089.
69. Kutschej, K.; Mayrhofer, P.H.; Kathrein, M.; et al. Structure, Mechanical and Tribological Properties of Sputtered $Ti_{1-x}Al_xN$ Coatings with $0.5 \leq x \leq 0.75$. *Surf. Coat. Technol.* **2005**, *200*, 2358–2365. https://doi.org/10.1016/j.surfcoat.2004.12.008.
70. Holmberg, K.; Laukkanen, A.; Ronkainen, H.; et al. Tribological Contact Analysis of a Rigid Ball Sliding on a Hard Coated Surface: Part I: Modelling Stresses and Strains. *Surf. Coat. Technol.* **2006**, *200*, 3793–3809. https://doi.org/10.1016/j.surfcoat.2005.03.040.
71. Koshy, P.; Dewes, R.C.; Aspinwall, D.K. High Speed End Milling of Hardened AISI D2 Tool Steel (~58 HRC). *J. Mater. Process. Technol.* **2002**, *127*, 266–273. https://doi.org/10.1016/S0924-0136(02)00155-3.
72. Breidenstein, B.; Denkena, B. Significance of Residual Stress in PVD-Coated Carbide Cutting Tools. *CIRP Ann.* **2013**, *62*, 67–70. https://doi.org/10.1016/j.cirp.2013.03.101.
73. Outeiro, J.C.; Pina, J.C.; M'Saoubi, R.; et al. Analysis of Residual Stresses Induced by Dry Turning of Difficult-to-Machine Materials. *CIRP Ann.* **2008**, *57*, 77–80. https://doi.org/10.1016/j.cirp.2008.03.076.
74. Ulutan, D.; Ozel, T. Machining Induced Surface Integrity in Titanium and Nickel Alloys: A Review. *Int. J. Mach. Tools Manuf.* **2011**, *51*, 250–280. https://doi.org/10.1016/j.ijmachtools.2010.11.003.
75. Özel, T.; Zeren, E. Finite Element Method Simulation of Machining of AISI 1045 Steel with a Round Edge Cutting Tool. In Proceedings of the 8th CIRP International Workshop on Modelling of Machining Operations, Chemnitz, Germany, 10–11 May 2005; pp. 533–542.

76. Fernández-Abia, A.I.; Barreiro, J.; López de Lacalle, L.N.; et al. Behaviour of Austenitic Stainless Steels at High Speed Turning Using Specific Force Coefficients. *Int. J. Adv. Manuf. Technol.* **2012**, *62*, 505–515. https://doi.org/10.1007/s00170-011-3846-9.
77. Hovsepian, P.E.; Luo, Q.; Robinson, G.; et al. TiAlN/VN Superlattice Structured PVD Coatings: A New Alternative in Machining of Aluminium Alloys for Aerospace and Automotive Components. *Surf. Coat. Technol.* **2006**, *201*, 265–272. https://doi.org/10.1016/j.surfcoat.2005.11.106.
78. Münz, W.-D.; Donohue, L.A.; Hovsepian, P.Eh. Properties of Various Large-Scale Fabricated TiAlN- and CrN-Based Superlattice Coatings Grown by Combined Cathodic Arc–Unbalanced Magnetron Sputter Deposition. *Surf. Coat. Technol.* **2000**, *125*, 269–277. https://doi.org/10.1016/S0257-8972(99)00572-1.
79. Klocke, F.; Brinksmeier, E.; Weinert, K. Capability Profile of Hard Cutting and Grinding Processes. *CIRP Ann.* **2005**, *54*, 22–45. https://doi.org/10.1016/S0007-8506(07)60018-3.
80. Beatrice, B.A.; Kirubakaran, E.; Thangaiah, P.R.; et al. Surface Roughness Prediction Using Artificial Neural Network in Hard Turning of AISI H13 Steel with Minimal Cutting Fluid Application. *Procedia Eng.* **2014**, *97*, 205–211. https://doi.org/10.1016/j.proeng.2014.12.243.
81. Bobzin, K.; Brögelmann, T.; Kalscheuer, C. Triboactive CrAlN+X Hybrid dcMS/HPPMS PVD Nitride Hard Coatings for Friction and Wear Reduction on Components. *Surf. Coat. Technol.* **2017**, *332*, 452–463. https://doi.org/10.1016/j.surfcoat.2017.06.089.
82. Franz, R.; Mitterer, C. Vanadium Containing Self-Adaptive Low-Friction Hard Coatings for High-Temperature Applications: A Review. *Surf. Coat. Technol.* **2013**, *228*, 1–13. https://doi.org/10.1016/j.surfcoat.2013.04.034.
83. Bobzin, K.; Brögelmann, T.; Kruppe, N.C.; et al. Nanocomposite (Ti,Al,Cr,Si)N HPPMS Coatings for High Performance Cutting Tools. *Surf. Coat. Technol.* **2019**, *378*, 124952. https://doi.org/10.1016/j.surfcoat.2019.07.073.
84. Baptista, A.; Silva, F.J.G.; Porteiro, J.; et al. Sputtering Physical Vapour Deposition (PVD) Coatings: A Critical Review on Process Improvement and Market Trend Demands. *Coatings* **2018**, *8*, 402. https://doi.org/10.3390/coatings8110402.
85. Rachbauer, R.; Stergar, E.; Massl, S.; et al. Three-Dimensional Atom Probe Investigations of Ti–Al–N Thin Films. *Scr. Mater.* **2009**, *61*, 725–728. https://doi.org/10.1016/j.scriptamat.2009.06.015.
86. Musil, J. Hard Nanocomposite Coatings: Thermal Stability, Oxidation Resistance and Toughness. *Surf. Coat. Technol.* **2012**, *207*, 50–65. https://doi.org/10.1016/j.surfcoat.2012.05.073.
87. Hörling, A.; Hultman, L.; Odén, M.; et al. Mechanical Properties and Machining Performance of $Ti_{1-x}Al_xN$-Coated Cutting Tools. *Surf. Coat. Technol.* **2005**, *191*, 384–392. https://doi.org/10.1016/j.surfcoat.2004.04.056.
88. Veprek, S.; Veprek-Heijman, M.G.J. The Formation and Role of Interfaces in Superhard nc-MeN/a-Si_3N_4 Nanocomposites. *Surf. Coat. Technol.* **2007**, *201*, 6064–6070. https://doi.org/10.1016/j.surfcoat.2006.08.112.
89. Li, Z.; Munroe, P.; Jiang, Z.T.; et al. Designing Superhard, Self-Toughening CrAlN Coatings through Grain Boundary Engineering. *Acta Mater.* **2012**, *60*, 5735–5744. https://doi.org/10.1016/j.actamat.2012.06.049.
90. Paulitsch, J.; Schenkel, M.; Zufraß, T.; et al. Structure and Properties of High Power Impulse Magnetron Sputtering and DC Magnetron Sputtering CrN and TiN Films Deposited in an Industrial Scale Unit. *Thin Solid Films* **2010**, *518*, 5558–5564. https://doi.org/10.1016/j.tsf.2010.05.062.
91. Ahlgren, M.; Blomqvist, H. Influence of Bias Variation on Residual Stress and Texture in TiAlN PVD Coatings. *Surf. Coat. Technol.* **2005**, *200*, 157–160. https://doi.org/10.1016/j.surfcoat.2005.02.078.
92. Sarakinos, K.; Alami, J.; Konstantinidis, S. High Power Pulsed Magnetron Sputtering: A Review on Scientific and Engineering State of the Art. *Surf. Coat. Technol.* **2010**, *204*, 1661–1684. https://doi.org/10.1016/j.surfcoat.2009.11.013.
93. Kelly, P.J.; Arnell, R.D. Magnetron Sputtering: A Review of Recent Developments and Applications. *Vacuum* **2000**, *56*, 159–172. https://doi.org/10.1016/S0042-207X(99)00189-X.
94. Tillmann, W.; Grisales, D.; Stangier, D.; et al. Residual Stresses and Tribomechanical Behaviour of TiAlN and TiAlCN Monolayer and Multilayer Coatings by DCMS and HiPIMS. *Surf. Coat. Technol.* **2021**, *406*, 126664. https://doi.org/10.1016/j.surfcoat.2020.126664.
95. Abukhshim, N.A.; Mativenga, P.T.; Sheikh, M.A. Heat Generation and Temperature Prediction in Metal Cutting: A Review and Implications for High Speed Machining. *Int. J. Mach. Tools Manuf.* **2006**, *46*, 782–800. https://doi.org/10.1016/j.ijmachtools.2005.07.024.
96. Wang, J.; Liu, Z.; Wu, Y.; et al. Cutting Performance and Tool Wear of AlCrN- and TiAlN-Coated Carbide Tools during Milling of Tantalum–Tungsten Alloy. *Machines* **2024**, *12*, 170. https://doi.org/10.3390/machines12030170.
97. Bartkowiak, T.; Brown, C.A. Multiscale 3D Curvature Analysis of Processed Surface Textures of Aluminum Alloy 6061-T6. *Materials* **2019**, *12*, 257. https://doi.org/10.3390/ma12020257.
98. Wang, F.; Zhao, J.; Li, A.; et al. Effects of Cutting Conditions on Microhardness and Microstructure in High-Speed Milling of H13 Tool Steel. *Int. J. Adv. Manuf. Technol.* **2014**, *73*, 137–146. https://doi.org/10.1007/s00170-014-5812-9.
99. Bobzin, K.; Brögelmann, T.; Kruppe, N.C.; et al. Influence of HPPMS on Hybrid dcMS/HPPMS (Cr,Al)N Processes. *Surf. Coat. Technol.* **2019**, *358*, 57–66. https://doi.org/10.1016/j.surfcoat.2018.11.032.

100. Bouzakis, K.D.; Bouzakis, E.; Skordaris, G.; et al. Effect of PVD Films Wet Micro-Blasting by Various Al_2O_3 Grain Sizes on the Wear Behaviour of Coated Tools. *Surf. Coat. Technol.* **2011**, *205*, S128–S132. https://doi.org/10.1016/j.surfcoat.2011.03.046.
101. Kadam, G.S.; Pawade, R.S. Surface Integrity and Sustainability Assessment in High-Speed Machining of Inconel 718. *J. Clean. Prod.* **2017**, *147*, 273–283. https://doi.org/10.1016/j.jclepro.2017.01.104.
102. Beake, B.D.; Smith, J.F.; Gray, A.; et al. Investigating the Correlation between Nano-Impact Fracture Resistance and Hardness/Modulus Ratio from Nanoindentation at 25–500 °C and the Fracture Resistance and Lifetime of Cutting Tools with $Ti_{1-x}Al_xN$ (x = 0.5 and 0.67) PVD Coatings in Milling Operations. *Surf. Coat. Technol.* **2007**, *201*, 4585–4593. https://doi.org/10.1016/j.surfcoat.2006.09.118.
103. Tang, J.F.; Chen, I.H.; Lu, B.R.; et al. Effect of Bias Voltages and Interlayer Design on Microstructure, Mechanical Properties, and Adhesion Performance of AlCrSiN Coatings Deposited Using HiPIMS. *Surf. Coat. Technol.* **2024**, *480*, 130618. https://doi.org/10.1016/j.surfcoat.2024.130618.
104. Bouzakis, K.-D.; Bouzakis, E.; Kombogiannis, S.; et al. Effect of Cutting Edge Preparation of Coated Tools on Their Performance in Milling Various Materials. *CIRP J. Manuf. Sci. Technol.* **2014**, *7*, 264–273. https://doi.org/10.1016/j.cirpj.2014.05.003.
105. Bobzin, K.; Brögelmann, T.; Kruppe, N.C.; et al. Plastic Deformation Behavior of Nanostructured CrN/AlN Multilayer Coatings Deposited by Hybrid dcMS/HPPMS. *Surf. Coat. Technol.* **2017**, *332*, 253–261. https://doi.org/10.1016/j.surfcoat.2017.06.092.